Parallel Compression Is a Fast Low-Cost Assay for the High-Throughput Screening of Mechanosensory Cytoskeletal Proteins in Cells

Chunguang Miao,[†] Eric S. Schiffhauer,[‡] Evelyn I. Okeke,[‡] Douglas N. Robinson,[‡,§] and Tianzhi Luo*,[†,‡]

[†]CAS Key Laboratory of Mechanical Behavior and Design of Materials, Department of Modern Mechanics, University of Science and Technology of China, Hefei 230000, China

[‡]Departments of Cell Biology, Pharmacology and Molecular Medicine, and Medicine, School of Medicine, Johns Hopkins University, Baltimore, Maryland 21205, United States

[§]Department of Chemical and Biomolecular Engineering, Whiting School of Engineering, Johns Hopkins University, Baltimore, Maryland 21211, United States

S *Supporting Information*

ABSTRACT: Cellular mechanosensing is critical for many biological processes, including cell differentiation, proliferation, migration, and tissue morphogenesis. The actin cytoskeletal proteins play important roles in cellular mechanosensing. Many techniques have been used to investigate the mechanosensory behaviors of these proteins. However, a fast, low-cost assay for the quantitative characterization of these proteins is still lacking. Here, we demonstrate that compression assay using agarose overlay is suitable for the high throughput screening of mechanosensory proteins in live cells while requiring minimal experimental setup. We used several well-studied myosin II mutants to assess the compression assay. On the basis of elasticity theories, we simulated the mechanosensory accumulation of myosin II's and quantitatively reproduced the experimentally observed protein dynamics. Combining the compression assay with confocal microscopy, we monitored the polarization of myosin II oligomers at the subcellular level. The polarization was dependent on the ratio of the two principal strains of the cellular deformations. Finally, we demonstrated that this technique could be used on the investigation of other mechanosensory proteins.

KEYWORDS: *mechanosensing, mechanosensory accumulation, mechanotransduction, myosin II, actin filament, compression, mechanobiology*
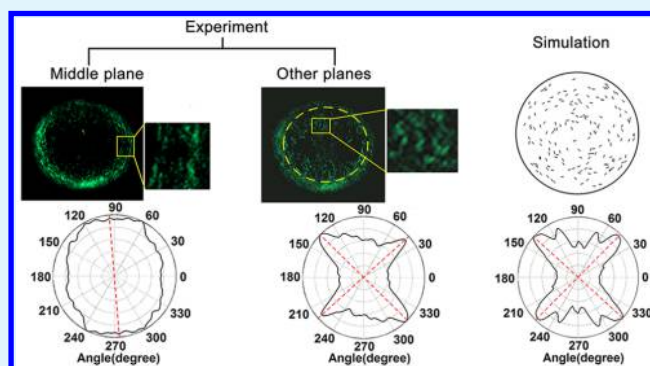
1. INTRODUCTION

Mechanosensing plays critical roles in many biological processes, such as cell differentiation, proliferation, migration, and tissue morphogenesis,[1,2] as well as physiological processes including blood flow regulation and lung respiration.[3] The actin cytoskeletal proteins in the cellular cortex are the major players that sense mechanical cues and activate downstream signaling pathways.[4,5] A quantitative understanding of the mechanosensing mechanisms of individual cytoskeletal proteins is essential for dissecting the role of these proteins in various signaling pathways and physiological systems.[6]

Due to the dynamic nature of the structure of actin cytoskeleton, it is challenging to quantitatively link the molecular mechanisms to cellular mechanosensing. As an active biomaterial, the actin cytoskeleton's network structure consists of proteins, including actin itself, actin cross-linking proteins (ACLP), and myosin II. At its core, actin monomers assemble into dynamic filaments with an average length of a few hundred nanometers; ACLPs cross-link the actin polymers into

networks. Myosin II, a motor protein, binds the actin filaments, pulling on them to generate contractile forces. On the basis of single-molecule measurements, the binding affinities of ACLPs and myosin II for actin filaments are force-dependent: Some of the binding lifetimes increase with force, and some decrease with force. All bonds eventually slip at high enough forces.[7,8] Thus, the microstructure of the actin cytoskeleton is highly dynamic due to the binding and unbinding events. More precisely, actin cytoskeleton is a smart material that continuously undergoes structural remodeling in response to mechanical stimuli.[9-13]

In recent decades, much effort has been invested in understanding the significance of the pathways of mechanosensing from molecular to cellular to tissue levels using both *in vivo* and *in vitro* assays.[10,11,13-17] At the cellular level, several
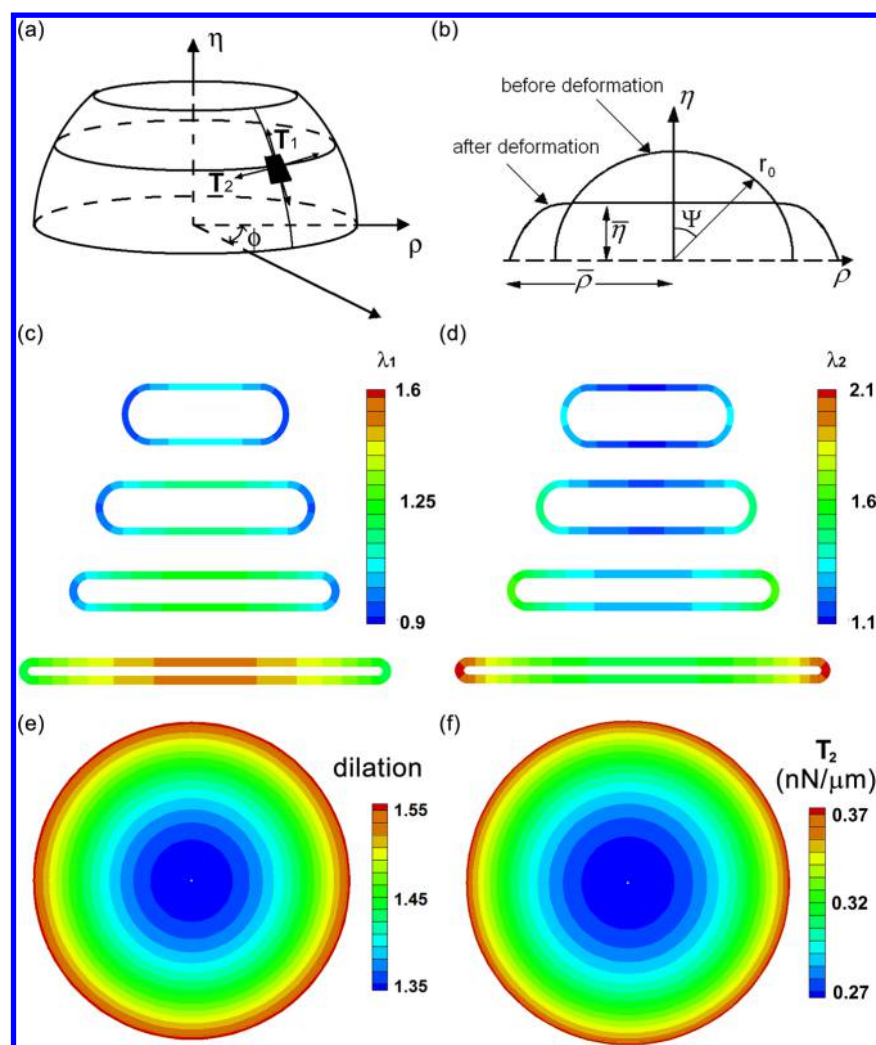
Figure 1. Deformations of a compressed cell: (a) Schematic graph of the principal strains and the associated coordination; (b) coordination after compression. Distribution of principal strain λ_1 (c) and λ_2 (d) at different compressed states λ_0 = 1.09, 1.16, 1.26, and 1.53 where λ_0 is the deformation at center of the contact region. The top views show the dilation (e) and the tension T_2 (f) for the case of λ_0 = 1.53. The subscripts 1 and 2 represent the meridional and circumferential directions, respectively.

experimental techniques have been used to quantify the mechanosensory behaviors of actin cytoskeletal proteins, such as micropipette aspiration, micropatterned substrates, parallel plate compression, and atomic force microscopy (AFM). Each assay has its own strengths and limitations. Among them, micropipette aspiration has been used extensively to characterize the force-dependent behaviors of actin cytoskeletal proteins in cells under different forces. This assay allows the mechanical loading on specific location of cell surface with a desired magnitude. For instance, this method has been used to obtain a mechanosensing landscape of actin cytoskeleton in *Dictyostelium* cells.[16,18,19] Specifically, it was discovered that different molecular structures of these proteins confer on them unique mechanosensitive properties: Proteins with rod-shaped backbone such as myosin II's and actinins are sensitive to dilation, while proteins forming V- (or Y)-shaped dimers such as filamins respond to shear deformation. However, this technique requires repeated iterations of the same measurement on many cells, one by one, to obtain statistically meaningful results, leading to a considerably large investment of the experimenter's time. Assays using micropatterned substrates are able to measure the cellular responses for many cells but involve

multiple microfabrication steps. Most of this kind of assays study the cell−substrate interactions triggered by the formation of focal adhesions, lacking the control of mechanical inputs.[17,20] Newly developed patterns such as magnetically actuated micropillars and cell-ladens allow for finely tuned mechanical stimuli by applying desired magnetic field.[21−23] Parallel plate compression and AFM use compression as mechanical stimuli for the investigation of cellular mechanobiology. These two methods do not require the activation of focal adhesion signaling pathway, but AFM can only measure one cell in an experiment. Parallel plate compression satisfies the need for large-scale measurement in a relatively short experimental period. Additionally, it offers convenient ways to vary the force on cells by either changing the total compression force or adjusting the cell density.

Over the years, various compression assays have been employed to characterize the mechanical properties of microcapsules, spherical core−shells made of mechano-responsive polymers, and live cells.[24,25] In these studies, nonlinear elasticity theories were introduced to predict the deformations of the core−shell structures under compression. Recently, compression assay using agar overlay has been

adopted in the investigations of mechanosensory behaviors of cytoskeletal proteins inside cells.[26,27] However, a quantitative interpretation of the protein behaviors based on the deformation of cells under compression is still absent. For example, the characterization of the mechanosensory behaviors of myosin II's in the published literature was more or less qualitative since the exact amount of compression on each cell was not well-defined and the dynamic responses of the proteins over time were not characterized.[26] Moreover, how the anisotropic deformations in a compressed cell affect the spatial distribution of the mechanosensitive proteins has not been fully investigated.

In this study, we used several well-studied myosin II mutants to test the ability of the compression assay for the characterizations of the mechanosensory responses of cytoskeletal proteins in many cells at one time. On the basis of elasticity theories, we calculated the tensions and strains along the cell cortex. Using this information as input, we simulated the mechanosensory accumulation of myosin II's and quantitatively reproduced the experimental observations. Combining the compression assay with confocal microscopy, we monitored the polarization of myosin II oligomers at the subcellular level. The polarization was found to be largely determined by the ratio of the two principal strains of the cellular deformations. Finally, we showed that this technique could be used for the investigation of other mechanosensory proteins. Our results demonstrated that the compression assay is a fast, low-cost technique for the high-throughput screening of mechanosensitive cytoskeletal proteins in cells.

2. MODELING AND SIMULATIONS

2.1. Calculation of the Principal Strains and Tensions of a Compressed Cell.
From a structural point of view, a weakly adherent cell can be considered to be a simplified sphere with a liquid core−cortical shell structure. The core is the cytoplasm with various organelles and can generally be treated as an incompressible viscous fluid with a constant volume. The shell is the membrane−cortex composite that behaves mechanically as a viscoelastic material that displays a strain-hardening or stress-relaxation behavior over different time scales.[11,28] To gain a quantitative understanding of the protein behaviors under compression, it is necessary to know the distribution of the stretching force on the shell. At this moment, we focus on the mechanical and chemical equilibrium of the cells first and neglect the time-dependence of its viscoelastic behaviors. Previously, theoretical analysis of the force distribution based on nonlinear elasticity was conducted on microcapsules.[29] Here, the cells of interest have a similar structure to that of the microcapsules although the constitutive equations and the mechanical properties of the materials are different. Additionally, it is expected that the force in the membrane-cortex of a compressed cell has a similar distribution. Considering the axial symmetry of a compressed cell, the mechanical equilibrium of the membrane−cortex composite can be described by two sets of equations: one for the contact region and the other for the noncontact region. The details of the derivation of these equations can be found in the work by Yang and Lardner.[30,31] The equations for the contact region are

$$\frac{d\lambda_1}{d\psi} = -\frac{\lambda_1}{\lambda_2 \sin \psi}\left(\frac{f_3}{f_1}\right) - \left(\frac{\lambda_1 - \lambda_2 \cos \psi}{\sin \psi}\right)\left(\frac{f_2}{f_1}\right) \tag{1}$$

$$\frac{d\lambda_2}{d\psi} = \frac{\lambda_1 - \lambda_2 \cos \psi}{\sin \psi} \tag{2}$$

where ψ is the angle measured from the vertical axis of symmetry (Figure 1a,b); λ_1 and λ_2 are the 2D principal stretches along the meridional and circumferential directions, respectively; and f_1, f_2, and

f_3 depend on the tensions and the materials properties (Supporting Information). The equations for the noncontact region are

$$\frac{d\lambda_1}{d\psi} = \left(\frac{\delta \cos \psi - \omega \sin \psi}{\sin^2 \psi}\right)\left(\frac{f_2}{f_1}\right) - \left(\frac{\omega}{\delta}\right)\left(\frac{f_3}{f_1}\right) \tag{3}$$

$$\delta = \lambda_2 \sin \psi \tag{4}$$

where $\omega = d\delta/d\Psi$. In addition, the relationship between ω and the pressure P is given by

$$\frac{d\omega}{d\psi} = \frac{d\lambda_1}{d\psi}\frac{\omega}{\lambda_1} + \left(\frac{\lambda_1^2 - \omega^2}{\delta}\right)\left(\frac{T_2}{T_1}\right) - \frac{\lambda_1(\lambda_1^2 - \omega^2)^{1/2} Pr_0}{T_1} \tag{5}$$

where r_0 is the radius of the cells and T_1 and T_2 are the tensions associated with λ_1 and λ_2, respectively. The governing eqs 1−5, along with their boundary conditions (Supporting Information), can be solved by a standard numerical scheme as the original boundary-value problem has been transformed into an initial value problem. A computer algorithm similar to that of Liu et al.[29] was developed to calculate the deformations with the prescribed deformation at $\psi = 0$ position (Figure S4). The Runge−Kutta method was used in the calculations to achieve high accuracy.

During the calculations of the strains and tensions, two types of materials have been considered: the neo-Hookean model and the STZC model.[32−34] The results based on STZC model are presented in the main text, whereas those calculated from neo-Hookean model are described in the Supporting Information.

2.2. Simulation of the Spatial Distribution of Myosin II's in a Compressed Cell.
Previously, the cellular accumulation of myosin II in response to micropipette aspiration was simulated by a set of partial differential equations where the force-dependency of myosin binding to actin and the cooperativity between bound myosin heads and the assembly of myosin II oligomers were taken into account.[18,19] Here, the assembly process is neglected for simplicity and the force-dependency is replaced with the dilation-dependency. In addition to the mass conservation, it is assumed that the dynamics of myosin II binding is described by

$$\frac{\partial C_{bound}}{\partial t} = D_1 \nabla^2 C_{bound} + k_{on}^{0} C_{actin} C_{unbound} - k_{off} C_{bound} \tag{6}$$

$$\frac{\partial C_{unbound}}{\partial t} = D_0 \nabla^2 C_{unbound} - k_{on}^{0} C_{actin} C_{unbound} + k_{off} C_{bound} \tag{7}$$

where $C_{unbound}$ and C_{bound} refer to the concentrations of unbound and bound myosin II, respectively; D_0 and D_1 are the diffusion coefficients for unbound and bound myosin II monomers, respectively; and k_{on}^{0} and k_{off} are the rate coefficients for binding and unbinding reactions, respectively. The initial concentration of myosin II is 3.0 μM.[35] The dilation dependency and cooperativity of myosin binding are incorporated into k_{off}:

$$k_{off} = k_{off}^{0} \exp\{-[k_{area}(\lambda_1\lambda_2 - 1) + \alpha C_{bound}]/k_B T\} \tag{8}$$

where k_{off}^{0} is the off-rate without dilation dependency and cooperativity; k_{area} is the sensitivity of myosin II to the area dilation (the term in the parentheses); α characterizes the strength of cooperativity; k_B is the Boltzmann constant; and T is the temperature. The ratio of k_{off}^{0} to k_{on}^{0} gives the dissociation rate k_d^{0}. In this study, k_{on}^{0} is fixed, while k_d^{0} varies between 0.3 and 0.7 μM by changing k_{off}^{0}.[36] The values of these parameters are summarized in Table 1. The principal strain parameters λ_1 and λ_2 are determined by eqs 1−5.

For the compressed cells in Figures 1 and S1, the partial differential eqs 6−8 are solved using a finite difference scheme. As the cell shape is symmetric with respect to the axis of revolution, the three-dimensional (3D) problem is solved in two dimensions (2D). Orthogonal curvilinear grids are generated to implement the numeric scheme.[37] The reflecting boundary condition is applied to the boundary nodes. It is assumed that the protein concentration in the cell cortex of

Table 1. Parameter Values Used in the Simulations

parameter	value	resource
C_{actin}	80.0 μM	35, 38
D_0	1.0–50.0 μm^2 s^{-1}	46
D_1	0.01–0.5 μm^2 s^{-1}	estimated ($D_1 = 0.01D_0$)
k_{on}^0	0.45 μM^{-1} s^{-1}	36, 70
k_{off}^0	0.14–0.31 s^{-1}	estimated
k_d^0	0.3–0.7 μM	36

thickness h has no gradient along the direction perpendicular to the cell surface.

3. METHODS AND MATERIALS

3.1. Cell Culture and Chemicals. Wild-type and mutant *Dictyostelium* strains were grown at 22 °C in Hans' Enriched HL-5 media. The details of the fluorescently tagged constructs for *Dictyostelium* cells were described in previous publications.[26,38,39] Plasmids encoding green fluorescent protein/red fluorescent protein/ yellow fluorescent protein (GFP/RFP/Citrine) fused to proteins of interest were transformed using electroporation and transformants were selected using the appropriate selection medium using Blasticidin S, G418, or Hygromycin.

NIH 3T3 cells were cultured in DMEM (Life Technology) with 10% FBS. GFP-tagged constructs for EGFP-C3-myoIIB were gifts from Dr. Robert Adelstein. Transient transfections of these plasmids were performed using FuGene HD (Promega).

3.2. Compression Assay. The cells were compressed between two parallel plates (shown in Figure S5). In our study, the top plate is a piece of transparent agarose gel, and the bottom plate is a piece of glass for microscope imaging. The surfaces of agarose gel and glass were not coated with any extra molecules. Agarose gel (2% weight) was cast into 150 μm thick sheet as described in Kee et al.[26] In brief, agarose powder was dissolved in boiled deionized (DI) water and the weight concentration was adjusted to 2%. The hot agarose solution was poured between two glass plates separated by 0.15 mm coverslips and cooled at room temperature. Subsequently, the agarose gels were transferred into DI water and stored at 4 °C for future use. Gels were kept for no more than 3 days to maintain their freshness. The tension tests were performed on agarose gels at room temperature using a LS materials testing machine (LS1, ANETEK, Inc.). The Young's modulus of 2% agarose gels extracted from the tension test curves is 310.2 ± 7.5 kPa, consistent with the reported values.[40] We plated the cells into an image chamber with a cross section of 10 mm × 40 mm. The bottom of the chamber was sealed by a piece of glass for imaging. For *Dictyostelium* cells, the imaging buffer was MES (2-(*N*-morpholino) ethanesulfonic acid) buffer (50 mM MES, pH 6.8, 2 mM MgCl$_2$, 0.2 mM CaCl$_2$), whereas DMEM was used for NIH 3T3 cells. After 5 min, most of the cells condensed to the bottom of the chamber and weakly adhered onto the glass substrate. Afterward, a piece of agarose gel was shaped into a size slightly smaller than the cross section of the chamber by a blade and was carefully loaded into the chamber without folding using a tweezer. To minimize the influence of buoyant forces, the imaging buffer in the chamber was removed by pipetting. Due to the gravitation of agarose gel, the cells underneath were compressed. For NIH 3T3 cells, the agarose overlay was conducted before the cells became spread on the substrate. It usually took 5 min for cells to change from a spherical to a pancake shape during compression. In such a short time window for measurement, the dehydration of agarose gels in the experiments was neglected.

One way to vary the force on each cell is to adjust the cell density while keeping the weight of the agarose gel fixed. Alternatively, one can keep the cell density fixed while changing the weight of the gel. By comparison, the former strategy is much easier to execute in experiments and was used in this study. The time-lapse of the cell shape change and the dynamics of fluorescent tagged actin cytoskeletal proteins were imaged using an Olympus IX81 inverted microscope. Using a 40× objective lens with bin 2, 200 cells can be measured in one experiment. The schematic diagrams of the fluorescent images of the corresponding undeformed and deformed cases are shown in Figure S5. Most of the fluorescent signals came from the 2D ring of the actin cortex that coincided with the focal plane of the microscope. The imaging window was 696 × 520 pixel^2, which corresponds to an area of 3.65 × 10^4 μm^2 on the substrate. The lowest cell density we used was 3 cells/image, which leads to the maximum force of 25 nN/ cell. However, one could define the smallest number per image as 1 cell. In that case, sometimes there were no cells in the imaging window because cells were not evenly distributed on the substrate, which dramatically increases the system error. Hence, we did not use cell cultures with very low cell density. The resulting force/cell was in the range of 0–25 nN, which is similar to those used in compression by atomic force microscopy.[41]

The images were processed by ImageJ software (imagej.nih.gov/ij). The lateral edges and the middle of the cells were outlined separately by the "Polygon selections" tool. The overall intensity of these parts was integrated by the "Measure" command and subsequently was divided by the corresponding areas to obtain the averaged intensity. The background intensity was subtracted from these intensities. The ratios were calculated by normalizing the lateral intensity against the middle intensity.

A Zeiss LSM 510 Meta confocal microscope was used to image the spatial distribution of myosin II and the volume change of the cells during compression. The step size along z direction was 200 nm, except in the rapid time-course assays of Figure S8, where the step size was 1 μm to reduce imaging time. During the time window for experiments, i.e., 5 min, the volume change was ~5% under compression regardless of the initial cell size (Figure S6), similar to the reported values for various mammalian cells.[42] Hence, the effect of the small change in volume during compression was neglected.

4. RESULTS AND DISCUSSION

During the compression of cells, the cell morphology and the dynamics of the fluorescent tagged proteins were monitored by microscopy. As the applied force by agarose overlay was calculated from the weight and cross-sectional area of the agarose sheet, we could correlate the accumulation of the mechanosensitive proteins to the applied force on each cell. To gain a quantitative understanding of the protein dynamics based the molecular mechanisms, it is necessary to know the exact amount of the local strains and tensions along the cell surface. However, these quantities are impossible to measure by current techniques and thus we utilize theoretical calculations to achieve good estimations.

We assumed that the cell behaves as a liquid core–cortical shell structure and that the cortical shell is a composite consisting of the plasma membrane and actin cytoskeleton. Previously, we demonstrated that the stiffness of cells is mostly governed by the actin cytoskeleton, not the plasma membrane, in both *in vivo* and *in vitro* experiments.[16] We used neo-Hookean and STZC models for the calculation of the principal tensions and strains of compressed cells.[32−34] The results in the main text are derived from STZC model, whereas the results based on neo-Hookean model are presented in the Supporting Information. The principal strains and tensions predicted by the STZC model are shown in Figure 1c−f. The strain along the circumferential direction (the same as T_2), λ_2, reaches its maximum at the lateral side (noncontact region), while it has its minimum at the center of top and bottom planes (the contact regions). In contrast, the strain along the meridional direction (the same as T_1), λ_1, decays along the path from the center of the contact region to the lateral edge. Importantly, the variation of λ_2 is larger than that of λ_1. Additionally, the area dilation at the lateral side is higher than that at the center of the contact region (Figure 1e) as is the tension along the circumferential
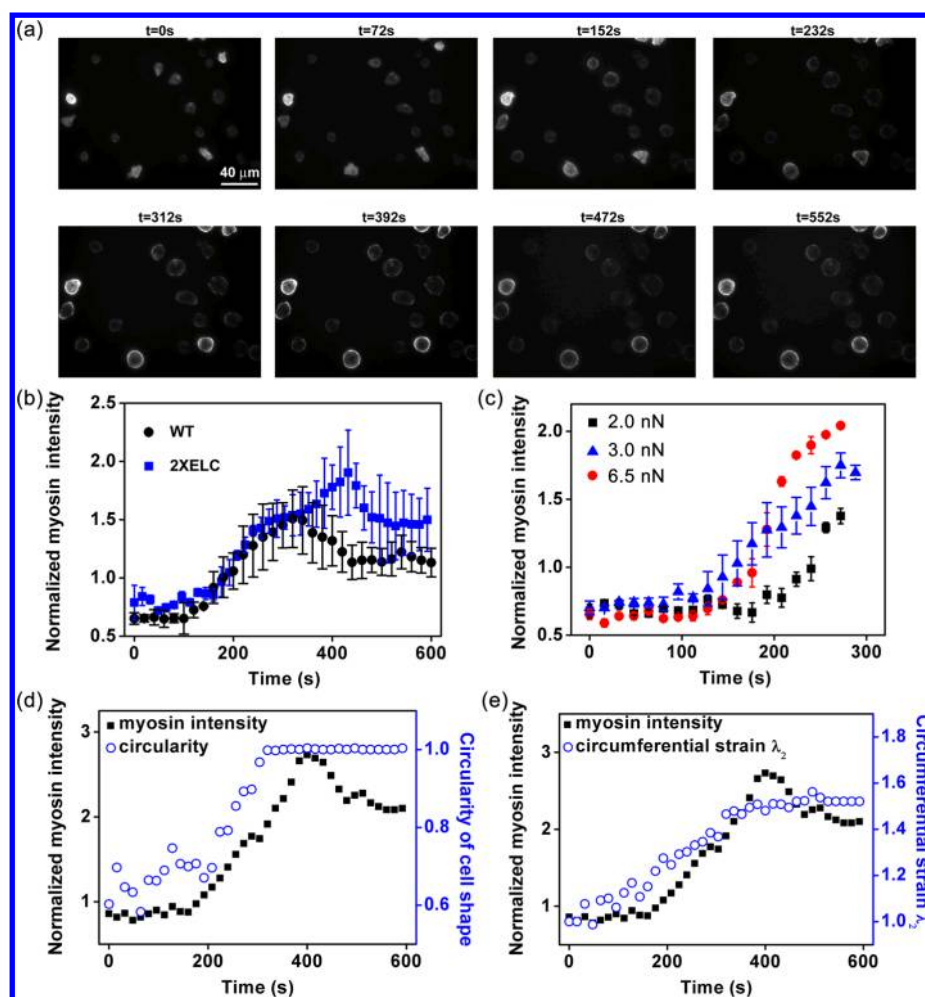
Figure 2. Experimentally observed dynamics of the accumulation of myosin II's in compressed cells: (a) Time lapse of the accumulation of myosin II 2xELC in multiple cells. (b) Dynamics of the accumulations of WT and 2xELC myosin II's. (c) Rising phase of the WT myosin II at the lateral edge under different compression forces 2.0, 3.0, and 6.5 nN. (d) Correlation between the myosin II intensity and the circularity of the middle plane of a compressed cell. (e) Correlation between the myosin II intensity and the circumferential strain λ_2. The error bars represent the standard error of mean.

direction (Figure 1f). The calculated quantities based on neo-Hookean model are similar (Figure S1) except that strain λ_1 increases along the path from the center of the contact region to the lateral side. Nevertheless, both models predict that the major dilation occurs at the lateral side.

The interaction between myosin II and actin is force-dependent.[8,43] Recently, we found that myosin II's are sensitive to dilation at the cellular level and accumulate to the dilated regions through diffusion: The 2xELC mutant with longer lever arm is very sensitive to mechanical stimuli. The ΔBLCBS mutant with the deletion of both light chains is less sensitive, and the S456L mutant with a point mutation near the adenosine triphosphate binding pocket has a sensitivity similar to that of the wild-type protein.[19,44] Consequently, the above theoretical results (Figure 1) imply that myosin II's are expected to accumulate to the lateral side of the compressed cells. Indeed, wild-type (WT) myosin II and its mutants displayed localized enrichment at the lateral edge in experiments. The time-lapse movies of compressed cells expressing Citrine-myosin II 2xELC showed dramatic increases of fluorescent signals at the lateral edge in a time window spanning ~5 min (Figure 2a). WT myosin II behaved similarly, but with slightly lower magnitude (Figure 2b). The

accumulations of both WT and 2xELC at the lateral side accelerated in the first 300 s and then decayed to plateaus. This acceleration is like the one we have observed in micropipette aspiration. The primary underlying mechanism is most likely the cooperative binding of neighboring myosin II heads to actin filaments.[18,44] Moreover, the magnitude of the accumulation of myosin II in the compression assay also increased with applied force (Figure 2c), which is similar to that observed in the micropipette aspiration assay. Interestingly, the middle plane of compressed cells became more circular over time, and we observed a strong correlation between the circularity of the cell shape and the myosin II accumulation (Figure 2d). Additionally, the strain of the circumference of the middle plane, λ_2, also correlated with the accumulation (Figure 2e). Here, λ_2 was calculated based on the change of the circumference. To prove that the accumulation is due to the intrinsic properties of myosin II but not actin flow or actin accumulation, we used GFP-actin and RFP-LimE to monitor the change of actin concentration during compression. We did not find any noticeable accumulations of actin (Figure 3a), which is similar to that in the mechanosensory measurement by micropipette aspiration.[19,44] Besides WT and 2xELC myosin II's, the ΔBLCBS and S456L mutant myosin II's also accumulated to
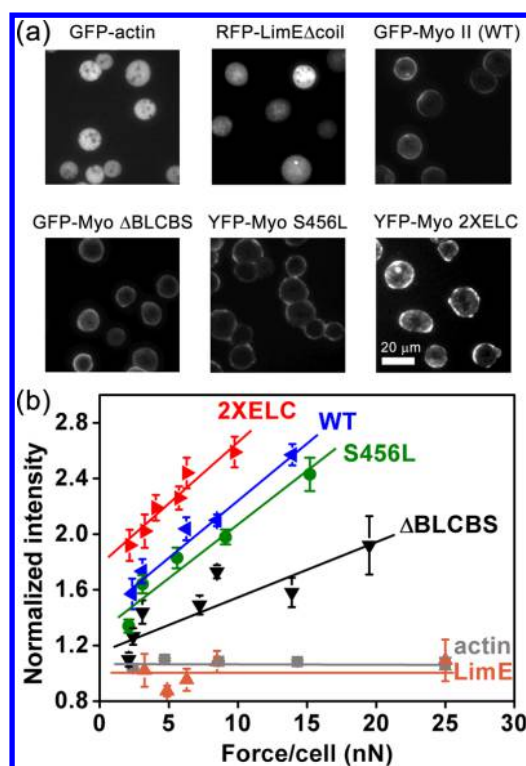
Figure 3. Force-dependent accumulation of myosin II's observed in experiments. (a) Snapshots of actin probes (GFP-actin and RFP-LimEΔcoil) and myosin II's (WT, ΔBLCBS, S456L, and 2xELC) were taken by epi-fluorescence microscopy. (b) Compared to actin and LimE, the peak intensities of the accumulation of different myosin II's displayed distinct trends in the force range of 0 to ~25 nN per cell. The lines only show the trends and are not fitted to the scattered points. The normalized intensity is the ratio between the fluorescence signals at the lateral edge and those in the middle of the cells. Mann−Whitney tests were performed between myosin II's and actin and the p-values are smaller than 0.01, indicating the myosin II's behaviors are statistically different from the actin. The error bars represent the standard error of mean.

the lateral edges of compressed cells, albeit to different degrees. To test if the compression assay could distinguish the mechanosensitivity of these proteins, we adjusted the applied force in the range of 0−25 nN/cell and measured the fluorescent signals of actin, LimE, WT, 2xELC, S456L, and ΔBLCBS (Figure 3b). Consistent with the results obtained by micropipette aspiration (Figure S7),[19,44] the accumulation of 2xELC myosin II displayed the highest accumulation over the force range, indicating it is very sensitive to the force change. WT and S456L ranked second and third, respectively. ΔBLCBS exhibited weakest mechanosensory response. Actin and LimE (a probe for actin turnover) did not show any force-dependent accumulations, suggesting that the mechanosensitive accumulation of myosin II during compression does not require local enrichment of actin or fast turnover of actin filament. This observation is further supported by the time-lapse images taken by confocal microscopy (Figure S8) where the GFP-myosin II and RFP-LimEΔcoil displayed distinct spatial distributions during compression. To further demonstrate that the force-dependent interaction between myosin II and actin filament is critical for the mechanosensitive accumulation of myosin II, we characterized the myosin II S1 behaviors using compression assay. Myosin II S1 lacks the assembly domain to form the bipolar thick filaments and cannot interact with actin filaments

in a force-dependent manner.[45] Therefore, this myosin mutant did not display any accumulations across the force range 0−25 nN/cell (Figure S9), which is significantly different from the other myosin II mutants. We note that blebbing occurs when the normalized myosin II intensity exceeds 3.0 due to strongly localized contractile forces. The data associated with blebbing were not included in our analysis because blebbing has a different underlying physical mechanism from the force-dependent mechanosensing.

To establish a quantitative linkage between myosin II accumulation and the cellular deformations, we examined the 3D distribution in the cell cortex. The spatial distribution of myosin II's in cells were measured by confocal microscopy. The top-view images (the upper row) in Figure 4a and b were made
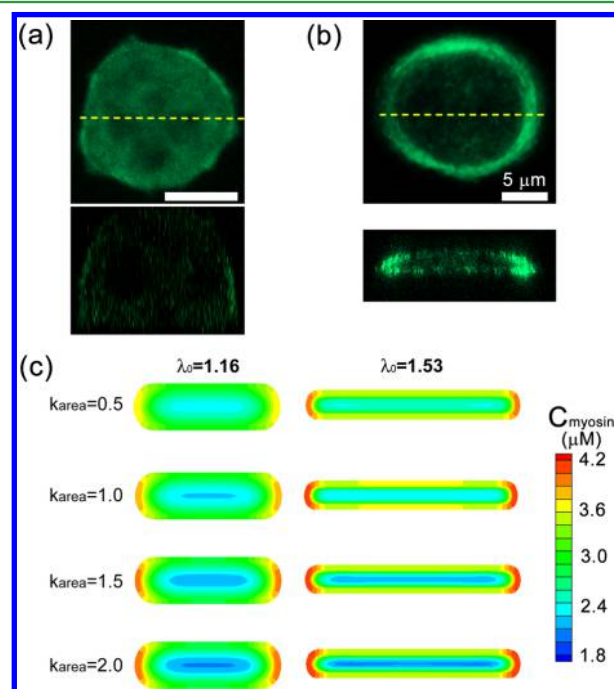

Figure 4. Spatial distribution of myosin II accumulation. The distribution of GFP-myosin II was imaged by confocal microscopy before (a) and after (b) compression. The upper row is the middle plane, whereas the lower row is the side view of planes indicated by yellow line. (c) The simulated myosin II intensity in compressed cells with different k_{area} (= 0.5, 1.0,, 1.5 and 2.0) at different compression states $\lambda_0 = 1.16$ (left column) and 1.53 (right column). For all cases, $D_0 = 1.0 \ \mu m^2/s$ and $k_d^0 = 0.5 \ \mu M$. Scale bars in all panels = 5 μm.

by projecting signals from different planes into one plane. Without compression, WT myosin II only displayed slight enrichment in the cortex (Figure 4a). After compression (Figure 4b and Movie S1), myosin II strongly accumulated to the lateral side. To further link the molecular mechanisms to the experimental observations, we simulated the distribution of myosin II's by solving a set of 3D reaction-diffusion equations in pancake-like geometries. We assumed that the binding of myosin II's to actin filaments is dilation-dependent. More specifically, the elastic energy associated with dilation increases the energy barrier for the unbinding reaction. In our model, the strength of dilation dependency is denoted by k_{area}. As shown in Figure 4c, a larger k_{area} leads to stronger accumulation for the given deformation λ_0; a larger deformation results in higher enrichment of myosin II for a given k_{area}. In fact, the simulated spatial distributions of myosin II match closely with the
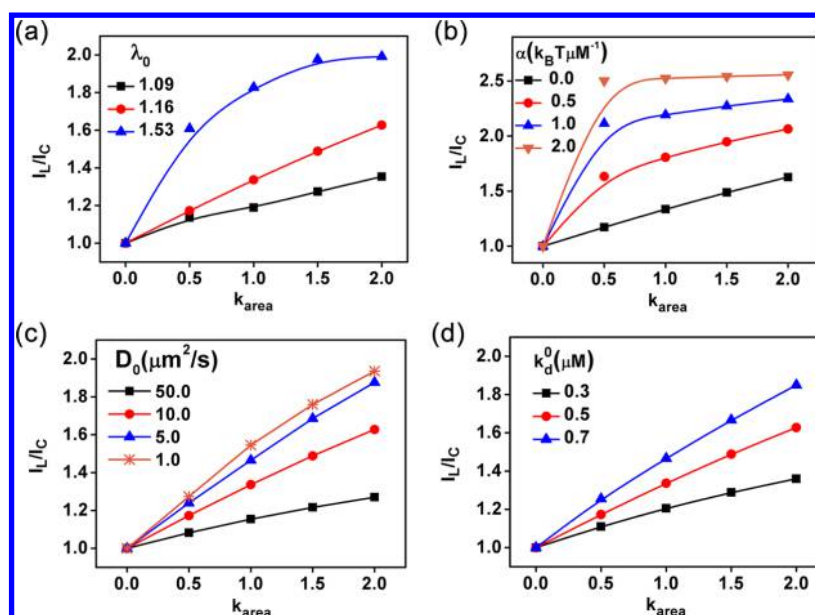
Figure 5. Simulated accumulation of myosin II for different λ_0 (a), α (b), D_0 (c), and k_d^0 (d). (a) $\alpha = 0.0$, $D_0 = 10.0\ \mu m^2/s$, and $k_d^0 = 0.5\ \mu M$. (b) $\lambda_0 = 1.16$, $D_0 = 10.0\ \mu m^2/s$, and $k_d^0 = 0.5\ \mu M$. (c), $\lambda_0 = 1.16$, $\alpha = 0.0$, and $k_d^0 = 0.5\ \mu M$. (d), $\lambda_0 = 1.16$, $\alpha = 0.0$, and $D_0 = 10.0\ \mu m^2/s$. I_L and I_C represent the concentrations of myosin II in the center and at the lateral side of a compressed cell, respectively.

experimental observations where myosin II is depleted at the center of cell body and myosin II is enriched in the lateral side of the cell (Figure 4b, lower panel; Figure 4c).

The comparison between simulations and experiments not only validates the predictive power of the physical model but also narrows down the range of the values of the parameters in the model, especially for those that are inaccessible to the experiments. In addition to the strains, several key parameters are also required in the dilation-dependent model, including the strength of cooperativity α, the sensitivity of myosin II to dilation k_{area}, the dissociation rate k_d^0, and the diffusion coefficients D_0 and D_1. Among them, D_0 was measured by fluorescence recovery after photobleaching (FRAP) and found to be ~0.8 $\mu m^2/s$;[46] D_1 was taken as $0.01D_0$ in previous studies.[8,23] The quantity of other parameters can be estimated by comparing the experimental observations to the simulation results. For instance, a typical value of λ_2 can be as high as 1.6 (Figure 2e), which sets the range of λ_0 since λ_0 is generally smaller than λ_2. In combination with the experimental observation that the magnitude of myosin II accumulations was between 1.0 and 2.5 (Figure 3b) the simulations predict k_{area} to be ~2.0 (Figure 5a) when $k_d^0 = 0.5\ \mu M$, $D_0 = 1.0\ \mu m^2/s$, and $\alpha = 1.0$. On the basis of this prediction, we conclude that the strength of cooperativity α has a value of ~1.0 (Figure 5b) when $k_d^0 = 0.5\ \mu M$, $D_0 = 1.0\ \mu m^2/s$, and $\lambda_0 = 1.16$. It is worth pointing out that different myosin II mutants are predicted to have slightly different k_{area} and α. At the molecular level, 2xELC is more sensitive to force than WT, whereas ΔBLCBS is less sensitive.[47] Here, the dilation-dependent model also predicts that protein with higher k_{area} is expected to display stronger accumulation during compression for given deformation, which is consistent with the experimental observations of myosin II mutants (Figure 3b). To compare the simulations to the experimental observations more directly, the simulated accumulations are plotted against the compression force (Figure S10b). Within the similar force range, the simulations quantitatively reproduce the trends of accumulation except for slight differences in the magnitude. Additionally, the accumu-

lation of myosin II converges as D_0 decreases from 50.0 to 1.0 $\mu m^2/s$ for $\lambda_0 = 1.16$, $k_d^0 = 0.5\ \mu M$, and $\alpha = 0.0$ (Figure 5c), suggesting that $D_0 = 1.0\ \mu m^2/s$ and $D_1 = 0.01D_0$ are reasonable choices for the dilation-dependent model. Moreover, a slight change of k_d^0 leads to significant variation of the accumulation of myosin II when $\lambda_0 = 1.16$, $D_0 = 1.0\ \mu m^2/s$, and $\alpha = 0.0$ (Figure 5d), indicating that the dilation-dependent model proposed here is very sensitive to the value of k_d^0. The sensitivity analysis of these four parameters in Figure 5 and its comparison to experiments demonstrate that the dilation-dependent reaction-diffusion equations with the chosen parameters quantitatively reflect the experimentally observed accumulation of myosin II during compression.

In addition to the spatial distribution of myosin II, the compression assay by agarose overlay also permits the observation of the evolution of its fine structures. The functional unit of myosin II is its oligomers, known as bipolar thick filaments (BTFs). The myosin heads stick out at the two ends of a BTF, while stacking their assembly domains in the middle. This type of structure allows the BTFs to generate contractile force in the actin network. The contractile force associated with one BTF at submicron scale is more or less like a force dipole often seen in condensed matter physics on the nanometer scale.[48] It is known that the structures formed by actin and myosin II's can change their patterns in response to local force (or tension).[49−52] One typical example is the stress fiber whose orientation tends to align with the principal stress direction.[53−57] Here, the orientation of myosin II's is random in an uncompressed cell since the tension is roughly isotropic. Upon compression, our theoretical results show that the principal tensions and strains along the circumferential direction are quite different from those along meridional direction (Figures 1, S1, and S2). Such anisotropy is expected to result in the change of BTFs' orientation. We used confocal microscopy to achieve high resolution of the BTFs. Indeed, BTFs in the middle plane where λ_2 and T_2 reached their maximums were aligned along the circumferential direction (the inset of Figure 6a), i.e., parallel to the T_2 or λ_2. If the
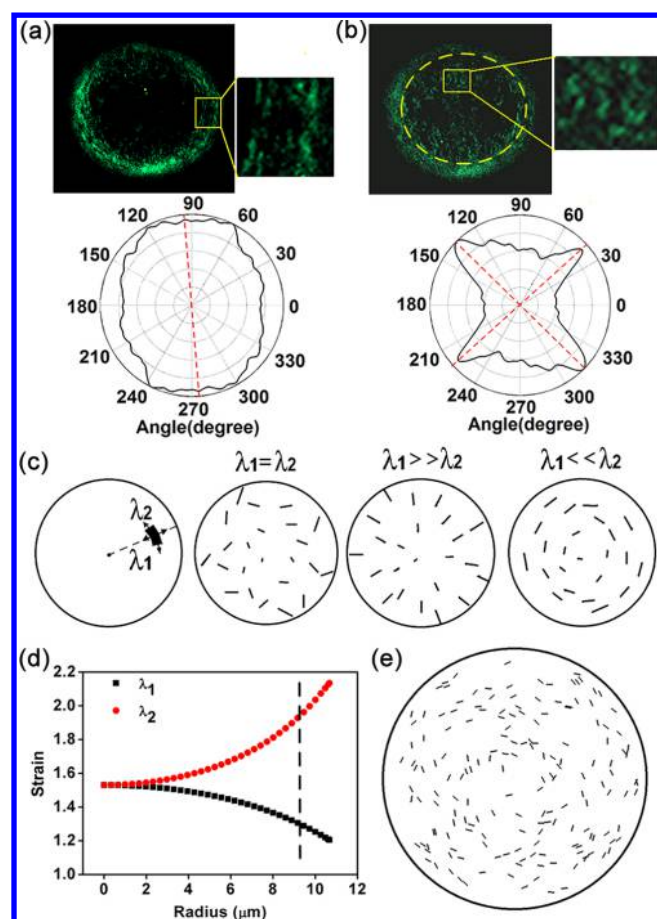
Figure 6. Polarization of myosin II BTFs due to the anisotropy of principal strains. (a) GFP-myosin II in the middle plane of a compressed cell was imaged by confocal microscopy (upper panel) and the angle distribution of the BTFs was statistically counted (low panel). (b) The fluorescence signals of myosin II were projected onto the middle plane (upper panel), and the angle distribution of the BTFs from other planes (circled by the dotted line) was statistically plotted (lower panel). (c) The polarization of myosin II BTFs was schematically illustrated for different anisotropy of the principal strains. (d) A typical example of the calculated principal strains projected on the middle plane was plotted as a function of the cell radius. The broken line is the boundary between the contact and noncontact regions. (e) The polarization of myosin II BTFs in the contact region was calculated based on the angle deviation $\xi = \tan^{-1}(\beta\lambda_2/\lambda_1)$ with $\beta = 4.0$. The inserts in (a) and (b) are zoom-in views indicated by the boxes.

fluorescent signals from other planes were projected to the middle plane, then a gradient of polarization of the BTFs was observed (inside the yellow circle of Figure 6b). Specifically, the orientation of the BTFs was random at the center, and it became more parallel to the circumferential direction at the position further away from the center. By comparison, the angle distribution of BTFs in the middle plane (lower panel of Figure 6a) has an averaged value about $\pm 90°$, whereas that of the BTFs from other plane peaks around $\pm 45°$ (lower panel of Figure 6b). To quantitatively interpret this phenomenon, we used a theory similar to the ones proposed by Nisenholz and Livne.[48,53] Since the polarization of BTFs is induced by the anisotropy of strains (or tensions), the angle of BTFs deviated away from the meridional direction was quantified by a parameter ξ that has a value of $\tan^{-1}(\beta\lambda_2/\lambda_1)$. Here, β is the coefficient that controls the effect of the ratio of the two

principal strains on ξ. As shown in the 2D schematic graphs (Figure 6c), the orientation of BTFs is about $\pm 45°$ with respect to the radical direction when $\lambda_1=\lambda_2$; it mostly points along the radical direction (along the meridional direction in 3D) when $\lambda_1 \gg \lambda_2$. On the contrary, it is parallel to the circumferential direction when $\lambda_1 \ll \lambda_2$. Actually, ξ is the angle of the orientation of one BTF with respect to the radical direction and has the value of ± 45, 0, and $\pm 90°$ for the above three special cases. For a compressed cell, λ_1 is almost equal to λ_2 in the center of contact area, i.e., the center of projected plane, whereas it becomes smaller than λ_2 as the position moves from the center to the border of the contact area (Figure 6d). Using the predicted strains as input, we calculated the orientation of the BTFs whose angles are based on the value of ξ. The simulated polarization pattern with moderate $\beta = 4$ (Figure 6e) is quite close the experimental observation (the yellow circle of Figure 6b). Specifically, the quantified angle distributions of these two are in good agreement (Figure S11), suggesting that the ratio between λ_1 and λ_2 indeed determines the orientation of the BTFs in cell cortex. The common feature of the compressed cells is that the BTFs tend to align with the circumferential direction as its position approaches the border of the contact area. Additionally, the simulations demonstrate that the orientation of BTFs becomes more parallel to the circumferential direction as β increases (Figure S12). Taken together, the combination of compression assay and confocal microscopy allows for detailed observation of the fine structures in actin cytoskeleton.

It is noted that the difference between the principal strains at the lateral edge calculated from STZC model (Figure 1c,d) is larger than that based on neo-Hookean model (Figures S1 and S2). According to the experimental observation (Figure 6a), the polarization of BTFs became more evident as its position approached the lateral edge where λ_2/λ_1 reaches its maximum. Significantly, almost all BTFs were aligned parallel to the circumferential direction, indicating that the difference between λ_2 and λ_1 indeed determines the polarization of BTFs. Thus, the small difference between the principal strains predicted by neo-Hookean model (Figure S3) is unable to explain the dramatic polarization pattern in the experiments and STZC model presents more reasonable interpretations. Actually, the inadequacy of neo-Hookean model for the large deformations of two-dimensional biomaterials has already been documented.[58] The main reason possibly lies in the STZC model being more nonlinear than neo-Hookean model, allowing the STZC model to closely capture the major features of the large deformation of biological materials.

At the molecular level, the polarization of myosin II BTFs shares a common underlying mechanism with the reorientation of stress fibers in adhere cells subjected to substrate stretching,[54,56] i.e., the force-dependent interaction between myosin II and actin filaments. However, these two processes are very different in several aspects: (1) The reorientation of stress fibers is usually associated with focal adhesions, but the change of polarization of BTFs does not require adhesion. (2) It often takes hours for the reorientation of stress fiber to complete, but the time scale of the change of the polarization of BTF is around a few minutes. (3) The cellular deformation under compression is much larger than that due to substrate stretching, which results in the need of different elasticity theories to calculate the deformations. (4) The adherent cells on stretched substrate are treated as 2D objects, whereas the cellular deformations due to compression are 3D. (5) The
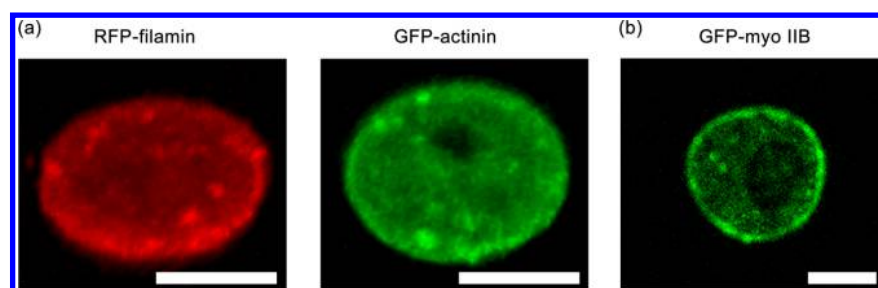
Figure 7. Accumulation of other actin cytoskeletal proteins in cells: (a) accumulations of filamin and α-actinin in compressed *racE* null and *myosin II* null *Dictyostelium* cells, respectively. Images were taken by confocal microscopy and combined into stacks (reproduced from Luo et al.,[19] permission from Nature Publisher); (b) accumulations of myosin IIB in compressed NIH 3T3 cells. Images were taken by epi-fluorescence microscopy. Scale bars in all panels = 10 μm.

applied force in compression assay is constant over time, but oscillated force is frequently employed in substrate stretching.

Apart from myosin II in *Dictyostelium* cells, ACLPs such as α-actinin and filamin also displayed accumulation at the lateral cortex upon compression (Figure 7a). Furthermore, the accumulation of myosin II's was also observed in mammalian cells such as NIH 3T3 cells (Figure 7b) where myosin IIB similarly displayed strong concentration at the lateral cortex. The mechanosensory behaviors of these proteins were consistent with our previous observations where they were systematically characterized by micropipette aspiration.[19,59] Therefore, the compression assay through agarose overlay is not only suitable for the characterization of myosin II's but also for other proteins. Additionally, the fact that filamin accumulated to the lateral side of a compressed cell where the shear strain (the difference between λ_2 (Figure 1d) and λ_1 (Figure 1c) reaches its maximum is consistent with the previous observations that filamin is sensitive to the shear deformation, but the compression assay is not able to distinguish the sensitivity of these proteins to different deformations since both dilation and shear deformations have their maximum values at the lateral edges of a compressed cell.

It is worth pointing out that both neo-Hookean model and STZC model assume that the materials have relative simple stress−strain relations. However, the actin cytoskeleton displayed strain-hardening behaviors and its stress−strain relation has a power-law character.[11,28,60,61] Additionally, we assumed that the actin cytoskeleton was homogeneous in our modeling and simulations and the viscosity of the cell deformation was negligible, yet the accumulation of myosin II and ACLPs observed in experiments suggests that the local protein concentration, the microstructure of actin cytoskeleton, and the corresponding mechanical properties evolved during deformation. Despite the limitations of these assumptions, our modeling and simulation results present a quantitative interpretation of the experimentally observed accumulation of cytoskeletal proteins.

So far, we have demonstrated that a compression assay can be used to deform many cells at one time while allowing for real-time monitoring of the mechanosensory behaviors of cytoskeletal proteins as well as the cell shape change. The accumulation of myosin II's and the polarization of BTFs could be quantitatively interpreted by the corresponding molecular mechanisms, cellular mechanics, and reaction−diffusion processes. Compared to the micropipette aspiration assay that exerts pulling force on cells, the compression assay by agarose overlay is low-cost because it does not require a specific apparatus, such as a water tank and micropositioning system

that are essential to micropipette aspiration. Moreover, it provides a simultaneous measurement for many cells, whereas micropipette aspiration only tests one cell per measurement. For example, in this study, we could measure 200 cells at one time. Recently, AFM has also been used to characterize the mechanosensory behaviors of myosin II by compressing the cell body and dragging the cell edge, but it also suffers from the same limitations of low throughput and itself is a relatively expensive instrument.[62,63] Magnetically actuated patterns were also developed to probing the mechanosensitive responses of cells. This type of assay involves using the photolithographic technique to fabricate magnetically actuated micropillars and cell-ladens to generate local mechanical stimuli by applying desired magnetic field.[21−23] Similar to the compression assay by agarose overlay, it is able to measure many cells at one time but it needs multiple microfabrication steps. Nevertheless, all of these assays are able to apply several tens of nN forces on cells.

As the deformations during compression macroscopically occur through height reduction and in-plane expansion, the size variation of the cells potentially contributes to the experimental error. It is desired to gain an estimation of this error as it can be evaluated theoretically. On the basis of the geometrical analysis, the strain variations ($\delta\lambda_1$ and $\delta\lambda_2$) are proportional to $\delta r/r_0$ where δr denotes the variation of cell radius r_0. It was reported that δr of *Dictyostelium* cells is about 0.09 μm, while the averaged cell size is around 5 μm,[64] which sets $\delta r/r_0 \approx 0.02$. Consequently, $\delta\lambda_1$ and $\delta\lambda_2$ are about 0.02. For STZC model, the calculated tension variations δT_1 and δT_2 scale with $(\delta\lambda)^2$, resulting in the variation of tensions about 0.0004. As to 3T3 cells, experimentally measured values for r_0 and δr are 9.65 and 0.18 μm, respectively. It also leads to $\delta r/r_0 \approx 0.02$, close to that of *Dictyostelium* cells, indicating that the tension variations for 3T3 cells are also very small. Hence, the size variation mainly leads to a small error in the strain and tension calculations.

As shown above, cell size has a certain variation. One might think that the smaller cells could be compressed less, whereas the larger cells could be compressed more extensively, which leads to a size-dependent accumulation. To rule out the possibility that the accumulations of myosin II's in response to compression in Figure 3 is due to the cell size variation, we plotted the mechanosensitive accumulation of WT myosin II against the 2D projected area of the compressed cells (Figure S13). Here, the projected area is the measure of the cell volume because the cell shape is close to a pancake and the heights of the cells are the same. For two different load conditions (force/cell = 3.7 and 9.3 nN), the correlation coefficients are very small (nearly 0), indicating an absence of correlation between cell volume and myosin II accumulation. These results also

indicate that the factors contributing to the experimental errors include not only the cell size variation but others parameters such as protein expression level.

In the experiments, we manually removed the imaging buffer by pipetting. However, this approach always leaves some residual buffer around the cells, and these residues do not noticeably affect our measurements. First, the compression force on each cell is on the order of several nanonewtons, much larger than the capillary force associated with the buffer residues. A piece of evidence is that the cells lying in a dry imaging chamber do not change to pancakes over time in the absence of compression. Second, the buffer residues are almost the same around each cell when the cell density is varied, potentially resulting in a common baseline for all the experimental data. This baseline does not affect the slope for the measured behaviors of myosin II accumulations in response to compression. Third, the magnitude of cell compression and the subsequent mechanoresponse for cells seeded at similar densities upon media removal is similar across separate imaging events.

The removal of culture medium might lead to the swelling of the cells due to the unbalance of the osmotic pressures inside and outside of the cells. The consequence would be an increase in the tension of the whole cell cortex, which does not change the distribution of mechanosensitive proteins along the cortex due to the spherical symmetry of the cells. Thus, the removal of culture medium does not affect the comparison between the simulations and the experimental observations. In cells, there are many organelles besides the actin cytoskeleton. The large deformations during compression also change the shape of these organelles, such as nucleus envelope, mitochondria, and others. It was reported that the longtime deformation of nucleus envelope influence certain changes in gene expression.[65] Here, the time window of the experiments was relatively short, and we did not specifically monitor organellar dynamics. Nevertheless, we did notice that the number of contractile vacuoles increased during compression. The impact of the compression on the physiology of these organelles needs to be investigated in the future.

Many studies have investigated the mechanosensing of cytoskeletal proteins in the context of focal adhesions. In this study, the effect of the activation of adhesion pathways was negligible as the cells were compressed by two surfaces without any chemical modifications. In fact, the characteristic time for myosin II to accumulate during the compression assay is around 5 min, whereas it takes several hours for the stress fibers to reorient in cells subjected to substrate stretching where the reorientation is thought to be the result of the activation of focal adhesions.[54]

Gel-based assays have been shown previously to be highly suitable for large-scale cellular measurements. Dembo et al. investigated the traction force during cell migration on elastic substrates embedded with small marker particles.[66] Wang's lab studied the cell adhesion on flat polyacrylaminde substrates.[67] Chen's group used microfabricated arrays of elastomeric posts to quantitatively study the cell–substrate interaction.[17,20] Trepat's group developed a fluorescent marker-embedded polyacrylamide gel assay to detect the intercellular forces during collective cell migration and found that the cells migrate along the direction of maximal principal stress in the substrates.[68] Our study demonstrates the utility of agarose overlay for studying the mechanosensitive processes in cells. As agarose gel is not stable when the temperature is higher than 32

°C, we suggest using other gels that are more thermally stable at 37 °C for the study of the behaviors of mammalian cells.

5. CONCLUSIONS

We demonstrated that compression assay is a fast, low-cost technique for the high throughput screening of mechanosensitive cytoskeletal proteins in cells. Compared to other mechanical assays, this technique works in a similar force regime, while providing a quantitative measurement on multiple cells simultaneously with a minimal experimental setup. In combination with confocal microscopy, agarose overlay allows for the monitoring of the dynamics of cytoskeletal proteins at the subcellular level. This technique may be readily used with other tools, such as total internal reflection microscopy, fluorescence recovery after photobleaching, and fluorescence correlation spectroscopy, to lead to better understanding of the cellular mechanosensing and cell-matrix interactions.[27,69]

■ ASSOCIATED CONTENT

ⓈSupporting Information

The Supporting Information is available free of charge on the ACS Publications website at DOI: 10.1021/acsami.7b04622.

> Material models for the deformations of the cells subjected to parallel compression and supplementary figures (PDF)
>
> Movie S1 shows that after compression, myosin II strongly accumulated to the lateral side. (AVI)

■ AUTHOR INFORMATION

Corresponding Author

*E-mail: tzluo@ustc.edu.cn.

ORCID

Tianzhi Luo: 0000-0003-2637-9605

Notes

The authors declare no competing financial interest.

■ REFERENCES

(1) Geiger, B.; Spatz, J. P.; Bershadsky, A. D. Environmental Sensing through Focal Adhesions. *Nat. Rev. Mol. Cell Biol.* **2009**, *10* (1), 21–33.

(2) Engler, A. J.; Sen, S.; Sweeney, H. L.; Discher, D. E. Matrix Elasticity Directs Stem Cell Lineage Specification. *Cell* **2006**, *126*, 677–689.

(3) Prosser, B. L.; Ward, C. W.; Lederer, W. J. X-ROS Signaling: Rapid Mechano-chemo Transduction in Heart. *Science* **2011**, *333* (6048), 1440–1445.

(4) Jaalouk, D. E.; Lammerding, J. Mechanotransduction Gone Awry. *Nat. Rev. Mol. Cell Biol.* **2009**, *10* (1), 63–73.

(5) Friedl, P.; Gilmour, D. Collective Cell Migration in Morphogenesis, Regeneration and Cancer. *Nat. Rev. Mol. Cell Biol.* **2009**, *10* (7), 445−457.

(6) Vogel, V.; Sheetz, M. P. Local Force and Geometry Sensing Regulate Cell Functions. *Nat. Rev. Mol. Cell Biol.* **2006**, *7* (4), 265−275.

(7) Ferrer, J. M.; Lee, H.; Chen, J.; Pelz, B.; Nakamura, F.; Kamm, R. D.; Lang, M. J. Measuring Molecular Rupture Forces between Single Actin Filaments and Actin-binding Proteins. *Proc. Natl. Acad. Sci. U. S. A.* **2008**, *105*, 9221−9226.

(8) Kovacs, M.; Thirumurugan, K.; Knight, P. J.; Sellers, J. R. Load-dependent Mechanism of Nonmuscle Myosin 2. *Proc. Natl. Acad. Sci. U. S. A.* **2007**, *104*, 9994−9999.

(9) Kasza, K. E.; Rowat, A. C.; Liu, J.; Angelini, T. E.; Brangwynne, C. P.; Koenderink, G. H.; Weitz, D. A. The cell as a material. *Curr. Opin. Cell Biol.* **2007**, *19* (1), 101−107.

(10) Deng, L.; Trepat, X.; Butler, J. P.; Millet, E.; Morgan, K. G.; Weitz, D. A.; Fredberg, J. J. Fast and Slow Dynamics of the Cytoskeleton. *Nat. Mater.* **2006**, *5* (8), 636−640.

(11) Koenderink, G. H.; Dogic, Z.; Nakamura, F.; Bendix, P. M.; MacKintosh, F. C.; Hartwig, J. H.; Stossel, T. P.; Weitz, D. A. An Active Biopolymer Network Controlled by Molecular Motors. *Proc. Natl. Acad. Sci. U. S. A.* **2009**, *106* (36), 15192−15197.

(12) Janmey, P. A.; Weitz, D. A. Dealing with Mechanics: Mechanisms of Force Transduction in Cells. *Trends Biochem. Sci.* **2004**, *29* (7), 364−370.

(13) Chaudhuri, O.; Parekh, S. H.; Fletcher, D. A. Reversible Stress Softening of Actin Networks. *Nature* **2007**, *445*, 295−298.

(14) Wang, Y.; Botvinick, E. L.; Zhao, Y.; Berns, M. W.; Usami, S.; Tsien, R. Y.; Chien, S. Visualizing the Mechanical Activation of Src. *Nature* **2005**, *434*, 1040−1045.

(15) Köhler, S.; Schaller, V.; Bausch, A. R. Structure Formation in Active Networks. *Nat. Mater.* **2011**, *10* (6), 462−468.

(16) Luo, T.; Srivastava, V.; Ren, Y.; Robinson, D. N. Mimicking the Mechanical Properties of the Cell Cortex by the Self-assembly of an Actin Cortex in Vesicles. *Appl. Phys. Lett.* **2014**, *104* (15), 153701.

(17) Tan, J. L.; Tien, J.; Pirone, D. M.; Gray, D. S.; Bhadriraju, K.; Chen, C. S. Cells Lying on a Bed of Microneedles: An Approach to Isolate Mechanical Force. *Proc. Natl. Acad. Sci. U. S. A.* **2003**, *100* (4), 1484−1489.

(18) Luo, T.; Mohan, K.; Srivastava, V.; Ren, Y.; Iglesias, P. A.; Robinson, D. N. Understanding the Cooperative Interaction between Myosin II and Actin Cross-linkers Mediated by Actin Filaments during Mechanosensation. *Biophys. J.* **2012**, *102* (2), 238−247.

(19) Luo, T.; Mohan, K.; Iglesias, P. A.; Robinson, D. N. Molecular Mechanisms of Cellular Mechanosensing. *Nat. Mater.* **2013**, *12*, 1064−1071.

(20) Ricart, B. G.; Yang, M. T.; Hunter, C. A.; Chen, C. S.; Hammer, D. A. Measuring Traction Forces of Motile Dendritic Cells on Micropost Arrays. *Biophys. J.* **2011**, *101* (11), 2620−2628.

(21) Sniadecki, N. J.; Anguelouch, A.; Yang, M. T.; Lamb, C. M.; Liu, Z.; Kirschner, S. B.; Liu, Y.; Reich, D. H.; Chen, C. S. Magnetic Microposts as an Approach to Apply Forces to Living Cells. *Proc. Natl. Acad. Sci. U. S. A.* **2007**, *104* (37), 14553−14558.

(22) Li, Y.; Huang, G.; Gao, B.; Li, M.; Genin, G. M.; Lu, T. J.; Xu, F. Magnetically Actuated Cell-laden Microscale Hydrogels for Probing Strain-induced Cell Responses in Three Dimensions. *NPG Asia Mater.* **2016**, *8*, e238.

(23) Li, Y.; Huang, G.; Li, M.; Wang, L.; Elson, E. L.; Lu, T. J.; Genin, G. M.; Xu, F. An Approach to quantifying 3D Responses of Cells to Extreme Strain. *Sci. Rep.* **2016**, *6*, 19550.

(24) Davis, D. A.; Hamilton, A.; Yang, J.; Cremar, L. D.; Van Gough, D.; Potisek, S. L.; Ong, M. T.; Braun, P. V.; Martínez, T. J.; White, S. R.; Moore, J. S.; Sottos, N. R. Force-induced Activation of Covalent Bonds in Mechanoresponsive Polymeric Materials. *Nature* **2009**, *459*, 68−72.

(25) Marmottant, P.; Mgharbel, A.; Käfer, J.; Audren, B.; Rieu, J.-P.; Vial, J.-C.; van der Sanden, B.; Marée, A. F. M.; Graner, F.; Delanoë-Ayari, H. The Role of Fluctuations and Stress on the Effective Viscosity of Cell Aggregates. *Proc. Natl. Acad. Sci. U. S. A.* **2009**, *106* (41), 17271−17275.

(26) Kee, Y.-S.; Ren, Y.; Dorfman, D.; Iijima, M.; Firtel, R.; Iglesias, P. A.; Robinson, D. N. A Mechanosensory System Governs Myosin II Accumulation in Dividing Cells. *Mol. Biol. Cell* **2012**, *23*, 1510−1523.

(27) Ren, Y.; West-Foyle, H.; Surcel, A.; Miller, C.; Robinson, D. N. Genetic Suppression of a Phosphomimic Myosin II Identifies System-level Factors That Promote Myosin II Cleavage Furrow Accumulation. *Mol. Biol. Cell* **2014**, *25*, 4150−4165.

(28) Gardel, M. L.; Shin, J. H.; MacKintosh, F. C.; Mahadevan, L.; Matsudaira, P.; Weitz, D. A. Elastic Behavior of Cross-linked and Bundled Actin Networks. *Science* **2004**, *304*, 1301−1305.

(29) Liu, K. K.; Williams, D. R.; Briscoe, B. J. Compressive Deformation of a Single Microcapsule. *Phys. Rev. E: Stat. Phys., Plasmas, Fluids, Relat. Interdiscip. Top.* **1996**, *54* (6), 6673−6680.

(30) Feng, W. W.; Yang, W.-H. On the Contact Problem of an Inflated Spherical Nonlinear Membrane. *J. Appl. Mech.* **1973**, *40*, 209−214.

(31) Lardner, T. J.; Pujara, P. On the Contact Problem of a Highly Inflated Spherical Nonlinear Membrane. *J. Appl. Mech.* **1978**, *45*, 202−203.

(32) Mooney, M. A Theory of Large Elastic Deformation. *J. Appl. Phys.* **1940**, *11*, 582−592.

(33) Skalak, R.; Tozeren, A.; Zarda, R. P.; Chien, S. Strain Energy Function of Red Blood Cell Membrane. *Biophys. J.* **1973**, *13*, 245−264.

(34) Rivlin, R. S. Large Elastic Deformations of Isotropic Materials. I. Fundamental Concepts. *Philos. Trans. R. Soc., A* **1948**, *240* (822), 459−490.

(35) Surcel, A.; Kee, Y.-S.; Luo, T.; Robinson, D. N. Cytokinesis through Biochemical-Mechanical Feedback Loops. *Semin. Cell Dev. Biol.* **2010**, *21* (9), 866−873.

(36) Takács, B.; O'Neall-Hennessey, E.; Hetényi, C.; Kardos, J.; Szent-Györgyi, A. G.; Kovács, M. Myosin Cleft Closure Determines the Energetics of the Actomyosin Interaction. *FASEB J.* **2011**, *25* (1), 111−121.

(37) Thompson, J. F.; Warsi, Z. U. A.; Mastin, C. W. *Numerical Grid Generation: Foundation and Application*; Elsevier Science Publishing Co. Inc.: New York, 1985.

(38) Reichl, E. M.; Ren, Y.; Morphew, M. K.; Delannoy, M.; Effler, J. C.; Girard, K. D.; Divi, S.; Iglesias, P. A.; Kuo, S. C.; Robinson, D. N. Interactions between Myosin and Actin Crosslinkers Control Cytokinesis Contractility Dynamics and Mechanics. *Curr. Biol.* **2008**, *18* (7), 471−480.

(39) Effler, J. C.; Kee, Y.-S.; Berk, J. M.; Tran, M. N.; Iglesias, P. A.; Robinson, D. N. Mitosis-Specific Mechanosensing and Contractile Protein Redistribution Control Cell Shape. *Curr. Biol.* **2006**, *16* (19), 1962−1967.

(40) Normand, V.; Lootens, D. L.; Amici, E.; Plucknett, K. P.; Aymard, P. New Insight into Agarose Gel Mechanical Properties. *Biomacromolecules* **2000**, *1* (4), 730−738.

(41) Lulevich, V.; Zink, T.; Chen, H.-Y.; Liu, F.-T.; Liu, G.-y. Cell Mechanics Using Atomic Force Microscopy-based Single-cell Compression. *Langmuir* **2006**, *22*, 8151−8155.

(42) Hui, T. H.; Zhou, Z. L.; Qian, J.; Lin, Y.; Ngan, A. H. W.; Gao, H. Volumetric Deformation of Live Cells Induced by Pressure-activaed Corss-membrane Ion Transported. *Phys. Rev. Lett.* **2014**, *113* (11), 118101−118105.

(43) Veigel, C.; Molloy, J. E.; Schmitz, S.; Kendrick-Jones, J. Load-dependent Kinetics of Force Production by Smooth Muscle Myosin Measured with Optical Tweezers. *Nat. Cell Biol.* **2003**, *5* (11), 980−986.

(44) Ren, Y.; Effler, J. C.; Norstrom, M.; Luo, T.; Firtel, R. A.; Iglesias, P. A.; Rock, R. S.; Robinson, D. N. Mechanosensing through Cooperative Interactions between Myosin II and the Actin Crosslinker Cortexillin I. *Curr. Biol.* **2009**, *19* (17), 1421−1428.

(45) Toyoshima, Y. Y.; Kron, S. J.; McNally, E. M.; Niebling, K. R.; Toyoshima, C.; Spudich, J. A. Myosin Subfragment-1 Is Sufficient to Move Actin Filaments in Vitro. *Nature* **1987**, *328*, 536−539.

(46) Uehara, R.; Goshima, G.; Mabuchi, I.; Vale, R. D.; Spudich, J. A.; Griffis, E. R. Determinants of Myosin II Cortical Localization during Cytokinesis. *Curr. Biol.* **2010**, *20* (12), 1080−1085.

(47) Uyeda, T. Q.; Abramson, P. D.; Spudich, J. A. The Neck Region of the Myosin Motor Domain Acts as a Lever Arm to Generate Movement. *Proc. Natl. Acad. Sci. U. S. A.* **1996**, *93* (9), 4459−4464.

(48) Nisenholz, N.; Botton, M.; Zemel, A. Early-time Dynamics of Actomysoin Polarization in Cells of Confined Shape in Elastic Matrices. *Soft Matter* **2014**, *10*, 2453−2462.

(49) Théry, M.; Racine, V.; Pépin, A.; Piel, M.; Chen, Y.; Sibarita, J.-B.; Bornens, M. The Extracellular Matrix Guides the Orientation of the Cell Division Axis. *Nat. Cell Biol.* **2005**, *7* (10), 947−953.

(50) Burridge, K.; Wittchen, E. S. The Tension Mounts: Stress Fibers as Force-generating Mechanotransducers. *J. Cell Biol.* **2013**, *200* (1), 9−19.

(51) Chien, S. Mechanotransduction and Endothelial Cell Homeostasis: the Wisdom of the Cell. *Am. J. Physiol. Heart Circ. Physiol.* **2006**, *292* (3), H1209−H1224.

(52) Wang, J. H. C. Substrate Deformation Determines Actin Cytoskeleton Reorganization: A Mathematical Modeling and Experimental Study. *J. Theor. Biol.* **2000**, *202*, 33−41.

(53) Livne, A.; Bouchbinder, E.; Geiger, B. Cell Reorientation under Cyclic Stretching. *Nat. Commun.* **2014**, *5*, 3938.

(54) Kaunas, R.; Nguyen, P.; Usami, S.; Chien, S. Cooperative Effects of Rho and Mechanical Stretch on Stress Fiber Organization. *Proc. Natl. Acad. Sci. U. S. A.* **2005**, *102* (44), 15895−15900.

(55) Zemel, A.; Rehfeldt, F.; Brown, A. E. X.; Discher, D. E.; Safran, S. A. Optimal Matrix Rigidity for Stress-fibre Polarization in Stem Cells. *Nat. Phys.* **2010**, *6* (6), 468−473.

(56) Chen, B.; Chen, X.; Gao, H. Dynamics of Cellular Reorientation on a Substrate under Biaxial Cyclic Stretches. *Nano Lett.* **2015**, *15*, 5525−5529.

(57) Tojkander, S.; Gateva, G.; Lappalainen, P. Actin Stress Fibers-assembly, Dynamics and Biological Roles. *J. Cell Sci.* **2012**, *125*, 1855−1864.

(58) Bellini, C.; Glass, P.; Sitti, M.; Di Martino, E. S. Biaxial Mechanical Modeling of the Small Intestine. *J. Mech. Behav. Biomed. Mater.* **2011**, *4* (8), 1727−1740.

(59) Schiffhauer, E. S.; Luo, T.; Mohan, K.; Srivastava, V.; Qian, X.; Griffis, E. R.; Iglesias, P. A.; Robinson, D. N. Mechanoaccumulative Elements of the Mammalian Actin Cytoskeleton. *Curr. Biol.* **2016**, *26* (11), 1473−1479.

(60) Shin, J. H.; Gardel, M. L.; Mahadevan, L.; Matsudaira, P.; Weitz, D. A. Relating Microstructure to Rheology of a Bundled and Cross-linked F-actin Network in Vitro. *Proc. Natl. Acad. Sci. U. S. A.* **2004**, *101*, 9636−9641.

(61) Mizuno, D.; Tardin, C.; Schmidt, C. F.; MacKintosh, F. C. Nonequilibrium Mechanics of Active Cytoskeletal Networks. *Science* **2007**, *315*, 370−373.

(62) Kim, Ji H.; Ren, Y.; Ng, W. P.; Li, S.; Son, S.; Kee, Y.-S.; Zhang, S.; Zhang, G.; Fletcher, D. A.; Robinson, D. N.; Chen, E. H. Mechanical Tension Drives Cell Membrane Fusion. *Dev. Cell* **2015**, *32* (5), 561−573.

(63) Schillers, H.; Wälte, M.; Urbanova, K.; Oberleithner, H. Real-time Monitoring of Cell Elasticity Reveals Oscillating Myosin Activity. *Biophys. J.* **2010**, *99* (11), 3639−3646.

(64) Artemenko, Y.; Batsios, P.; Borleis, J.; Gagnon, Z.; Lee, J.; Rohlfs, M.; Sanséau, D.; Willard, S. S.; Schleicher, M.; Devreotes, P. N. Tumor Suppressor Hippo/MST1 Kinase Mediates Chemotaxis by Regulating Spreading and Adhesion. *Proc. Natl. Acad. Sci. U. S. A.* **2012**, *109* (34), 13632−13637.

(65) Swift, J.; Ivanovska, I. L.; Buxboim, A.; Harada, T.; Dingal, P. C. D. P.; Pinter, J.; Pajerowski, J. D.; Spinler, K. R.; Shin, J.-W.; Tewari, M.; Rehfeldt, F.; Speicher, D. W.; Discher, D. E. Nuclear Lamin-A Scales with Tissue Stiffness and Enhances Matrix-directed Differentiation. *Science* **2013**, *341* (6149), 1240104.

(66) Dembo, M.; Oliver, T.; Ishihara, A.; Jacobson, K. Imaging the Traction Stresses Exerted by Locomoting Cells with the Elastic Substratum Method. *Biophys. J.* **1996**, *70*, 2008−2022.

(67) Pelham, R. J.; Wang, Y.-L. Cell Locomotion and Focal Adhesions Are Regulated by Substrate Flexibility. *Proc. Natl. Acad. Sci. U. S. A.* **1997**, *94*, 13661−13665.

(68) Tambe, D. T.; Corey Hardin, C.; Angelini, T. E.; Rajendran, K.; Park, C. Y.; Serra-Picamal, X.; Zhou, E. H.; Zaman, M. H.; Butler, J. P.; Weitz, D. A.; Fredberg, J. J.; Trepat, X. Collective Cell Guidance by Cooperative Intercellular Forces. *Nat. Mater.* **2011**, *10* (6), 469−475.

(69) Srivastava, V.; Robinson, D. N. Mechanical Stress and Network Structure Drive Protein Dynamics during Cytokinesis. *Curr. Biol.* **2015**, *25* (5), 663−670.

(70) Murphy, C. T.; Spudich, J. A. Dictyostelium Myosin 25−50K Loop Substitutions Specifically Affect ADP Release Rates. *Biochemistry* **1998**, *37* (19), 6738−6744.

Supporting Information

Parallel compression is a fast, low-cost assay for the high throughput screening of mechanosensory cytoskeletal proteins in cells

Chunguang Miao,[a] Eric Schiffhauer,[b] Evelyn Okeke,[b] Douglas N. Robinson [b, c] and Tianzhi Luo,[a, b,*]

[a] CAS Key Laboratory of Mechanical Behavior and Design of Materials, Department of Modern Mechanics, University of Science and Technology of China, Hefei, China

[b] Department of Cell Biology, Pharmacology and Molecular Medicine, and Medicine, School of Medicine, Johns Hopkins University, Baltimore, MD, 21205, USA

[c] Department of Chemical and Biomolecular Engineering, Whiting School of Engineering, Johns Hopkins University, Baltimore, MD 21211, USA

* Correspondence: T. Luo at tzluo@ustc.edu.cn

1. Material models

For Mooney-Rivlin materials, the strain energy density, with a strain-hardening behavior can be described by the following simple form [1-2]:

$$W = C_1\left(\lambda_1^2 + \lambda_2^2 + \frac{1}{\lambda_1^2\lambda_2^2} - 3\right) + C_2\left(\lambda_1^2\lambda_2^2 + \frac{1}{\lambda_2^2} + \frac{1}{\lambda_1^2} - 3\right),$$
Eq. (S1)

where $C_1 = 6E_0$ and E_0 is the Young's modulus; C_2 is proportional to C_1 by a factor of β. As a result, the principal stresses are [3]

$$\sigma_1 = \lambda_1\frac{\partial W}{\partial \lambda_1} = 2C_1\left(\lambda_1^2 - \frac{1}{\lambda_1^2\lambda_2^2}\right)\left(1 + \beta\lambda_2^2\right),$$
Eq. (S2)

$$\sigma_2 = \lambda_2\frac{\partial W}{\partial \lambda_2} = 2C_1\left(\lambda_2^2 - \frac{1}{\lambda_1^2\lambda_2^2}\right)\left(1 + \beta\lambda_1^2\right).$$
Eq. (S3)

For a planar material with thickness of h, the corresponding tensions in the meridional and circumferential directions are

$$T_1 = \frac{h\sigma_1}{\lambda_1\lambda_2} = 2hC_1\left(\frac{\lambda_1}{\lambda_2} - \frac{1}{\lambda_1^3\lambda_2^3}\right)\left(1 + \beta\lambda_2^2\right),$$
Eq. (S4)

$$T_2 = \frac{h\sigma_2}{\lambda_1\lambda_2} = 2hC_1\left(\frac{\lambda_1}{\lambda_2} - \frac{1}{\lambda_1^3\lambda_2^3}\right)\left(1 + \beta\lambda_1^2\right).$$
Eq. (S5)

The corresponding f_i (i=1, 2, 3) are

$$f_1 = \frac{\partial T_1}{\partial \lambda_1} = 2hC_1\left(\frac{1}{\lambda_2} + \frac{3}{\lambda_1^4\lambda_2^3}\right)\left(1 + \beta\lambda_2^2\right),$$
Eq. (S6)

$$f_2 = \frac{\partial T_1}{\partial \lambda_2} = 2hC_1\left[\left(-\frac{\lambda_1}{\lambda_2^2} + \frac{3}{\lambda_1^3\lambda_2^4}\right)\left(1 + \beta\lambda_2^2\right) + 2\beta\lambda_2\left(\frac{\lambda_1}{\lambda_2} - \frac{1}{\lambda_1^3\lambda_2^3}\right)\right],$$
Eq. (S7)

$$f_3 = T_1 - T_2 = 2hC_1\left[\frac{\left(\lambda_1^2 - \lambda_2^2\right)}{\lambda_1\lambda_2} - \beta\left(\frac{1}{\lambda_1^3\lambda_2} - \frac{1}{\lambda_1\lambda_2^3}\right)\right].$$
Eq. (S8)

In this study, β was set to be 0 and the resulting equations constitute the well-known neo-Hookean model.

For STZC materials, the strain energy density has the form of [4]

$$W = \frac{B}{4}\left(\frac{1}{2}I_1{}^2 + I_1 - I_2\right) + \frac{C}{8}I_2{}^2,$$

Eq. (S9)

where B and C characterize material properties. In this study, $C=hE_0$ and $B=0.1C$. I_1 and I_2 are defined as:

$$I_1 = \lambda_1{}^2 + \lambda_2{}^2 - 2,$$

Eq. (S10)

$$I_2 = \lambda_1{}^2\lambda_2{}^2 - 1.$$

Eq. (S11)

The stress-strain relations are described by

$$T_1 = \frac{\lambda_1}{\lambda_2}\left[\frac{B}{2}\left(\lambda_1{}^2 - 1\right) + \frac{C}{2}\lambda_2{}^2 I_2\right],$$

Eq. (S12)

$$T_2 = \frac{\lambda_2}{\lambda_1}\left[\frac{B}{2}\left(\lambda_2{}^2 - 1\right) + \frac{C}{2}\lambda_1{}^2 I_2\right].$$

Eq. (S13)

The resulted f_i (i=1, 2, 3) are

$$f_1 = \frac{\partial T_1}{\partial \lambda_1} = \frac{\lambda_1}{2\lambda_2}\left[B\left(3\lambda_1 - \frac{1}{\lambda_1}\right) + C\lambda_2{}^2 I_2 + 2C\lambda_1\lambda_2{}^4\right],$$

Eq. (S14)

$$f_2 = \frac{\partial T_1}{\partial \lambda_2} = \frac{\lambda_1}{2}\left[-B\frac{\left(\lambda_1{}^2 - 1\right)}{\lambda_2{}^2} - CI_2 + 4C\lambda_1{}^2\lambda_2{}^2\right],$$

Eq. (S15)

$$f_3 = T_1 - T_2 = \frac{B}{2}\frac{\left(\lambda^2{}_1 - \lambda_2{}^2\right)\left(\lambda_1{}^2 + \lambda_2{}^2 + 1\right)}{\lambda_1\lambda_2}.$$

Eq. (S16)

2. Calculation of the deformations

For a compressed spherical shell by parallel plates, the deformation is symmetric and only half of the sphere needs to be considered. Defining $\boldsymbol{\Gamma}$ as the angle of the contact area (shown in **Fig. 1** in the main text), the boundary conditions are [3, 5]:

$$\psi = 0, \quad \lambda_1 = \lambda_2 = \lambda_0,$$

$$\psi = \Gamma, \quad \left(\lambda_1\right)_{contact} = \Gamma\left(\lambda_1\right)_{noncontact},$$

$$\psi = \Gamma, \quad \left(\lambda_2\right)_{contact} = \Gamma\left(\frac{\delta}{\sin\Gamma}\right)_{noncontact},$$

$$\psi = \Gamma, \quad \eta' = 0$$

$$\psi = \frac{\pi}{2}, \quad \delta' = 0,$$

where η is the direction perpendicular to the contact region and δ is the defined in Eq. 4.

Given the strain λ_0 in the center of the contact plane , the fourth order Runge-Kutta method was implemented to obtain T_1, T_2 , λ_1 and λ_2 by solving Eqs. (S4-8) or Eq. (S12-16). In the calculation of the deformations, the volume conservation and the boundary conditions described above were used [6]. The algorithm (shown in Fig. S3) is similar to the one developed by Liu *etc* [3]. The compression force F has a one-to-one correspondence to the strains as well as the cell height (**Fig. S5a**). Especially, the relation between $F/C_1 hr_0$ and $1-\eta/r_0$ can be described by a parabolic function for Mooney-Rivlin materials. As for STZC materials, the term $C_1 hr_0$ needs to be replaced with Bhr_0.

2. Supplementary figures
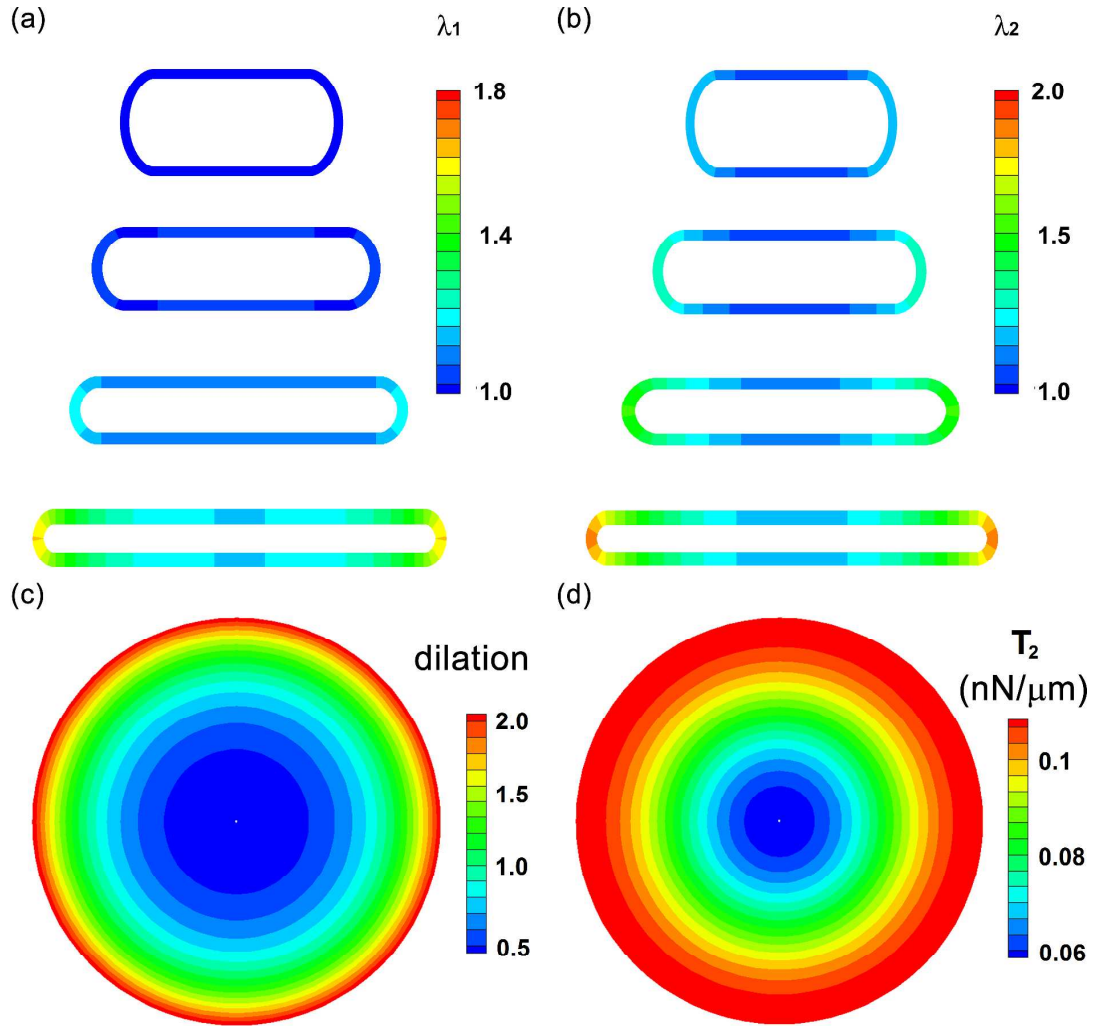
Figure S1. The principal strains of a neo-Hookean cell at different compressions. The strain λ_1 along the meridional direction **(a)** and the strain λ_2 along the circumferential direction **(b)** were calculated for λ_0 =1.00, 1.01, 1.06 and 1.16. The top-views of the dilation **(c)** and the tension T_2 along circumferential direction **(d)** of a compressed cell were plotted for λ_0= 1.16. The thickness h is 0.5 μm and Young's modulus E_0 is 10^2 Pa.
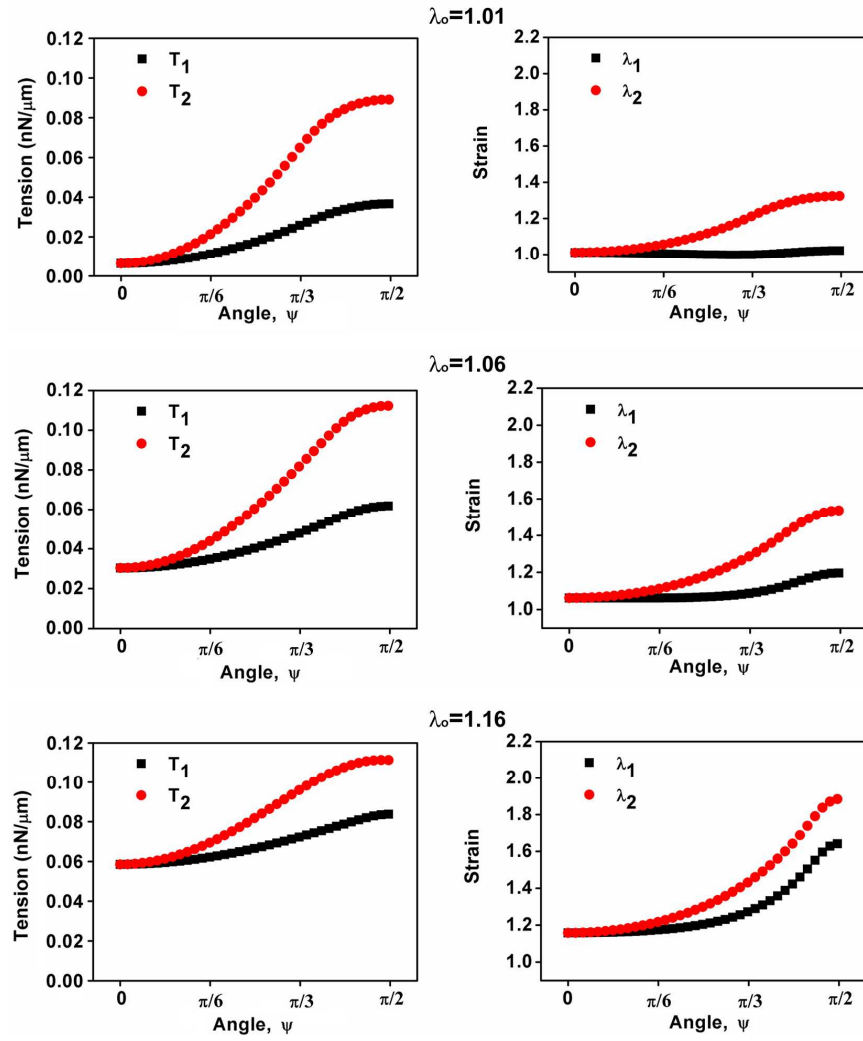
Figure S2. The tensions and strains along the two principal directions for a neo-Hookean cell under different compressions, *i.e.*, different λ_0 in the center of contact region. The thickness *h* is 0.5 μm and Young's modulus E_0 is 10^2 Pa.
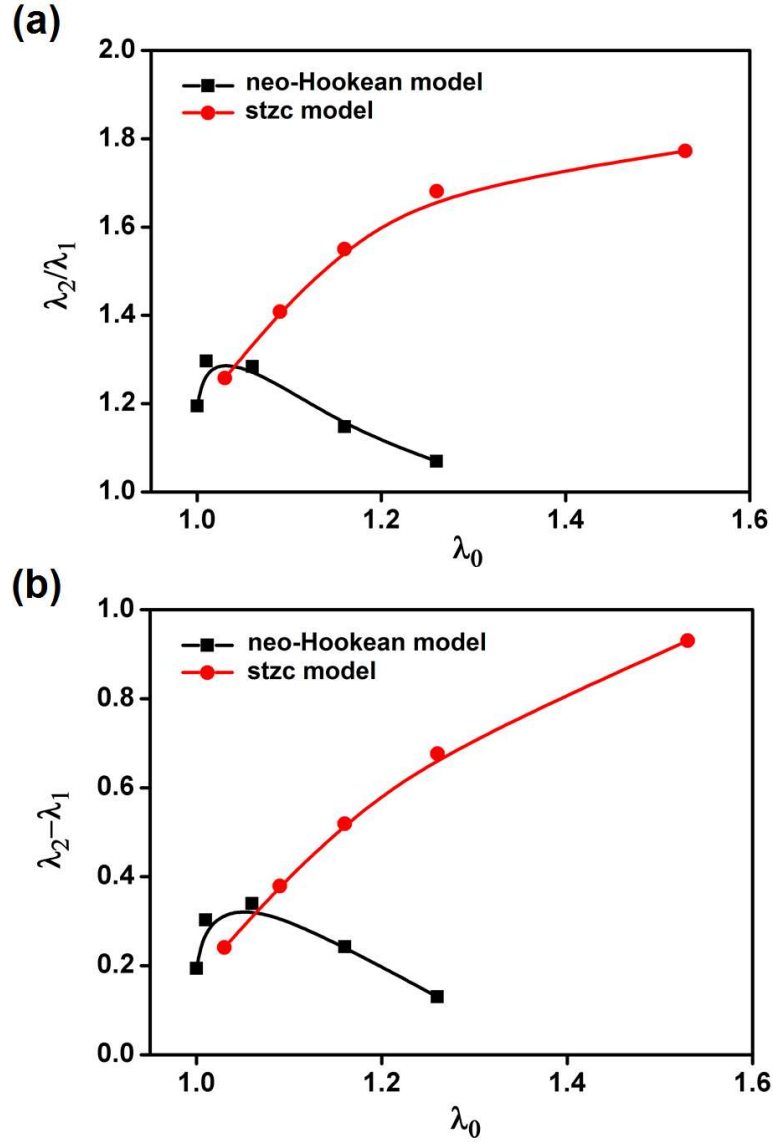
Figure S3. The ration (a) and difference (b) between the two principal strains (λ_1, λ_2) at the lateral edge of a compressed cell at different deformed states. The thickness h is 0.5 μm and Young's modulus E_0 is 10^2 Pa.
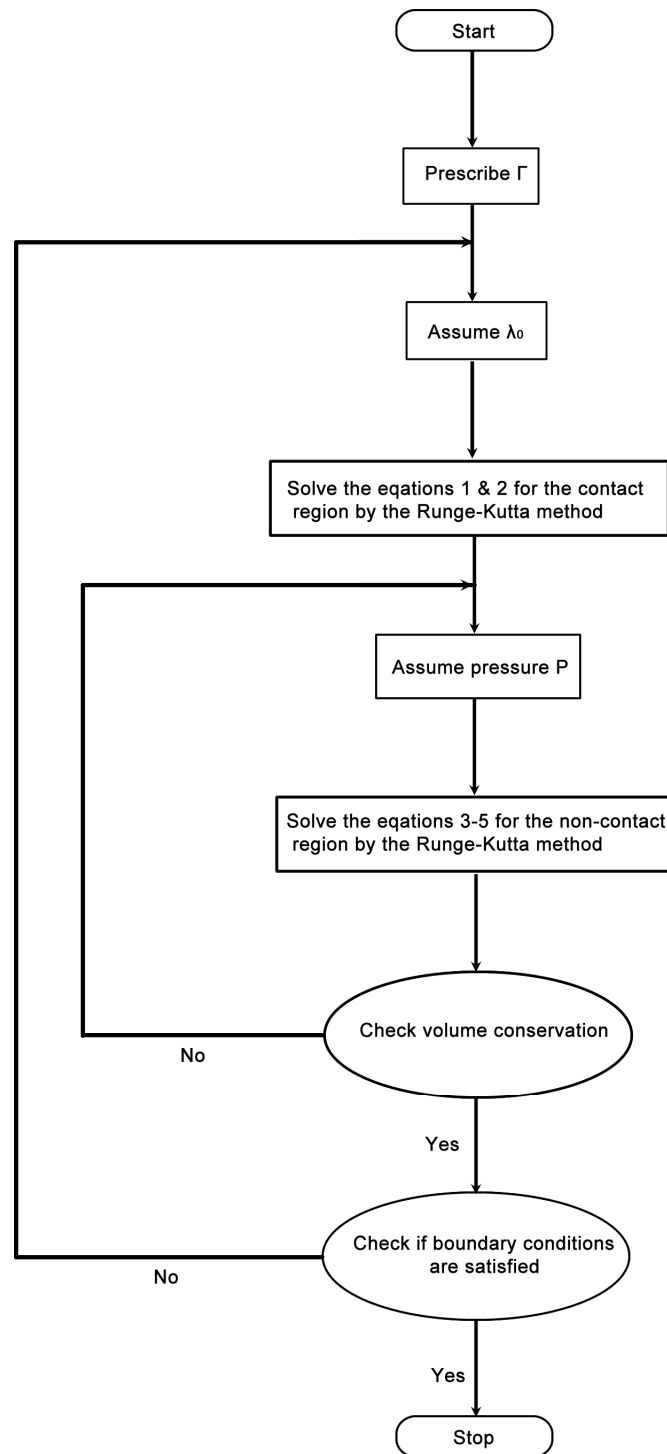
Figure S4. The flow chart of the algorithm for the calculation of the principal strains and tensions of a compressed cell.
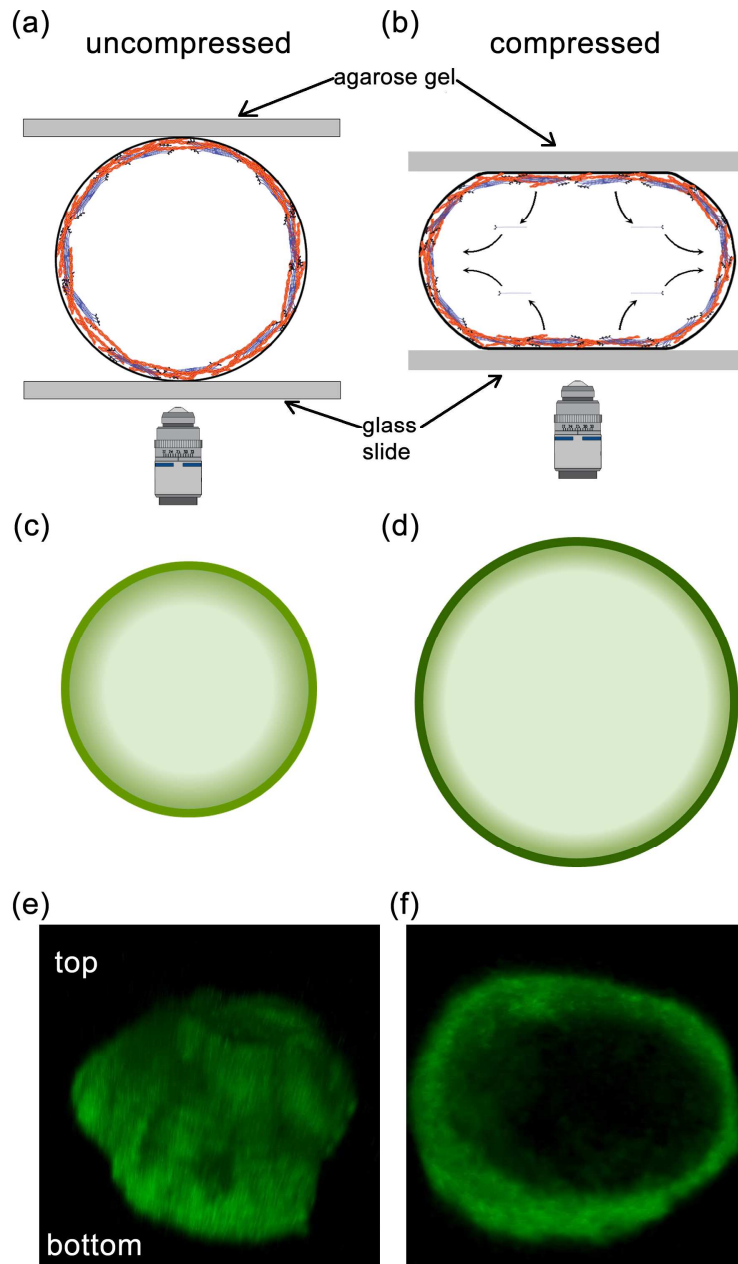
Figure S5. The strain induced accumulation of myosin II at the lateral side of a compressed cell through the reaction-diffusion process. The schematic views of uncompressed state **(a)** and compressed state **(b)**. The fluorescent signals were collected through the objective lens underneath the glass slide that seals the bottom of the imaging chamber. The illustration of the GFP-myosin II in the middle plane of a uncompressed **(c)** and compressed cell **(d)**, respectively. The experimental observation of the spatial distribution of GFP-myosin II in a uncompressed **(e)** and compressed **(f)** cell, respectively. The images in **(e)** and **(f)** were taken by confocal microscopy and reconstructed by stacking the images together.
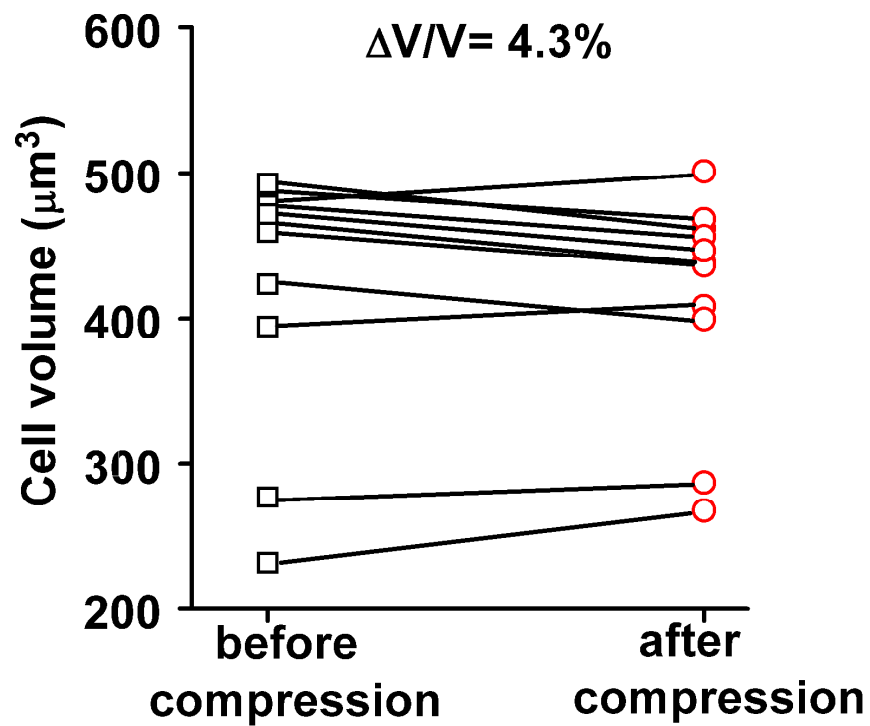
Figure S6. The volume change of *Dictyostelium* cells before and after compression measured by confocal microscopy. The experimental time-window for compression was about 5 minutes. The volume change was ±5%.
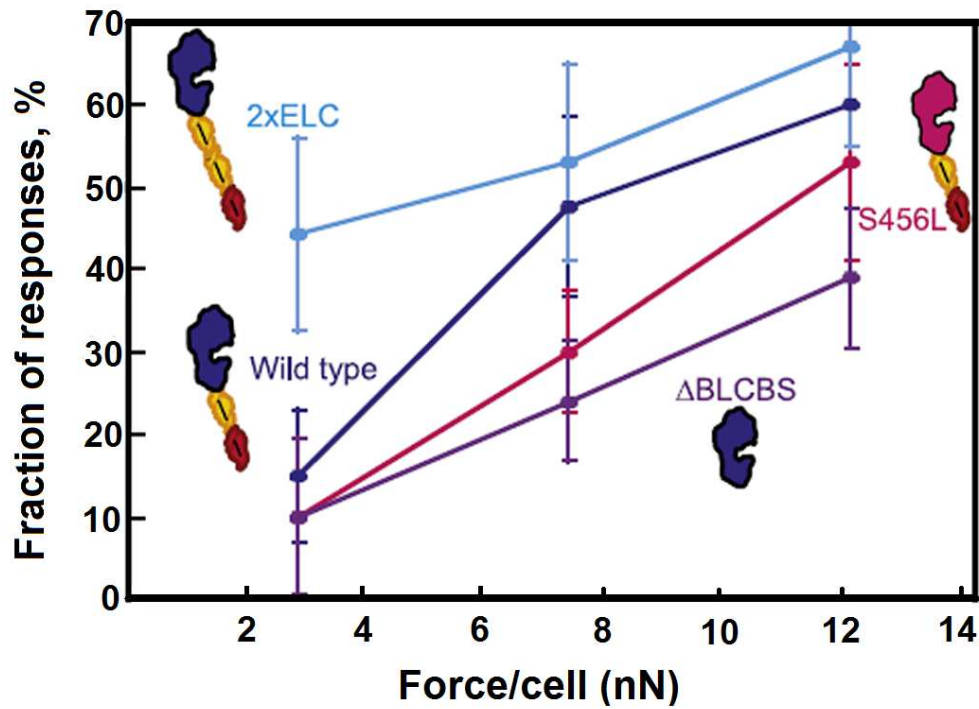
Figure S7. The mechanosensitive response of myosin IIs in *Dictyostelium* cells measured by micropipette aspiration (adapted from Ren *et al.*, *Current Biology*, 2009, 19:1421-1428, reproduced with permission from reference 44, copyright 2009 Elsevier Ltd). The force/cell was converted from the applied pressure provided that the micropipette radius was 2.5 μm in reference 44. Compared to the results in **Figure 3b**, the accumulations of the myosin IIs displayed similar trends within in the same force range.
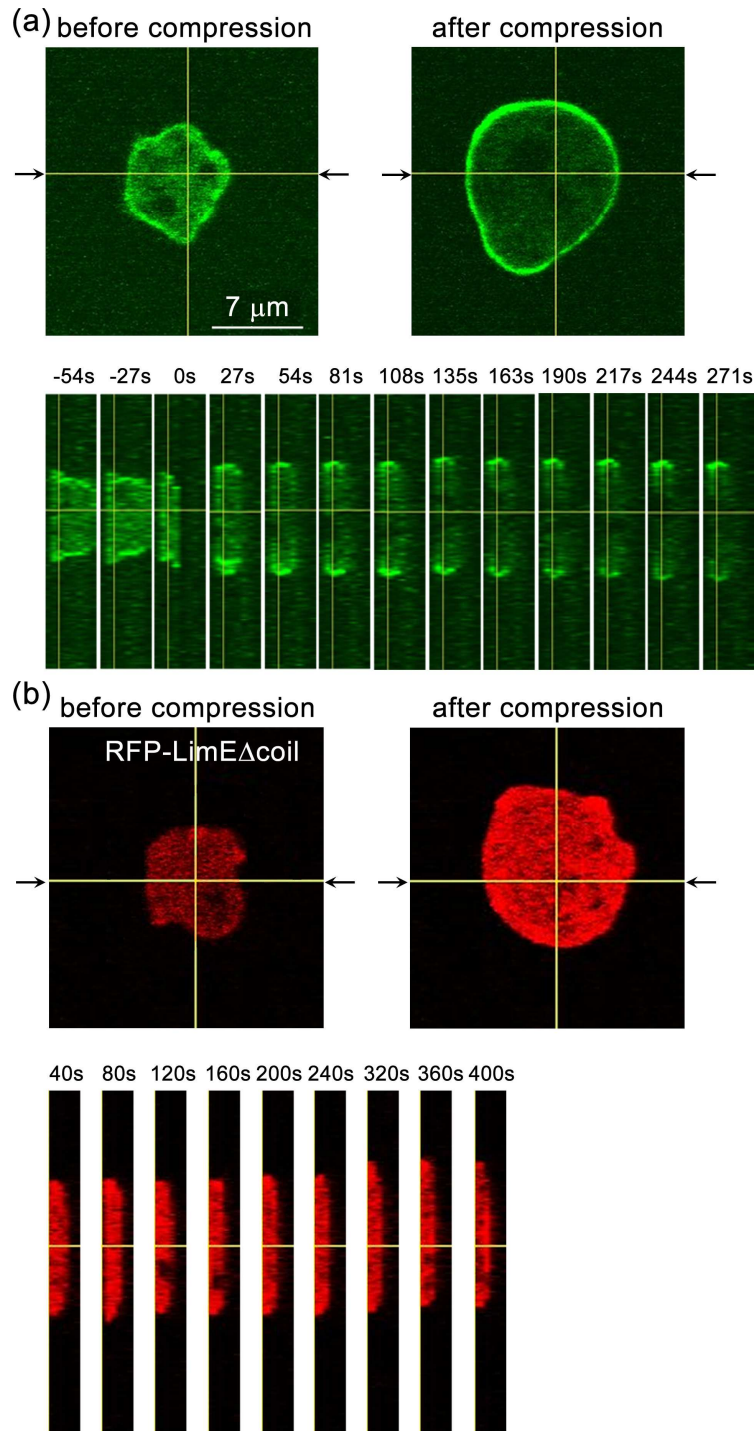
Figure S8. The time-lapse of compressed *Dictyostelium* cells expressing GFP-myosin II **(a)** and RFP-LimEΔcoil **(b)**, respectively, imaged by confocal microscopy. The upper row shows the distribution of the fluorescent proteins in x-y plane while the lower row displays the time-lapse of the protein distribution in x-z plane. The arrows in the upper row indicate the positions where the x-z planes are localized. The comparison between time-lapses of these two proteins suggests that myosin II and LimEΔcoil (an actin probe) have different spatial distributions. Scale bar in (a) applies to all images.
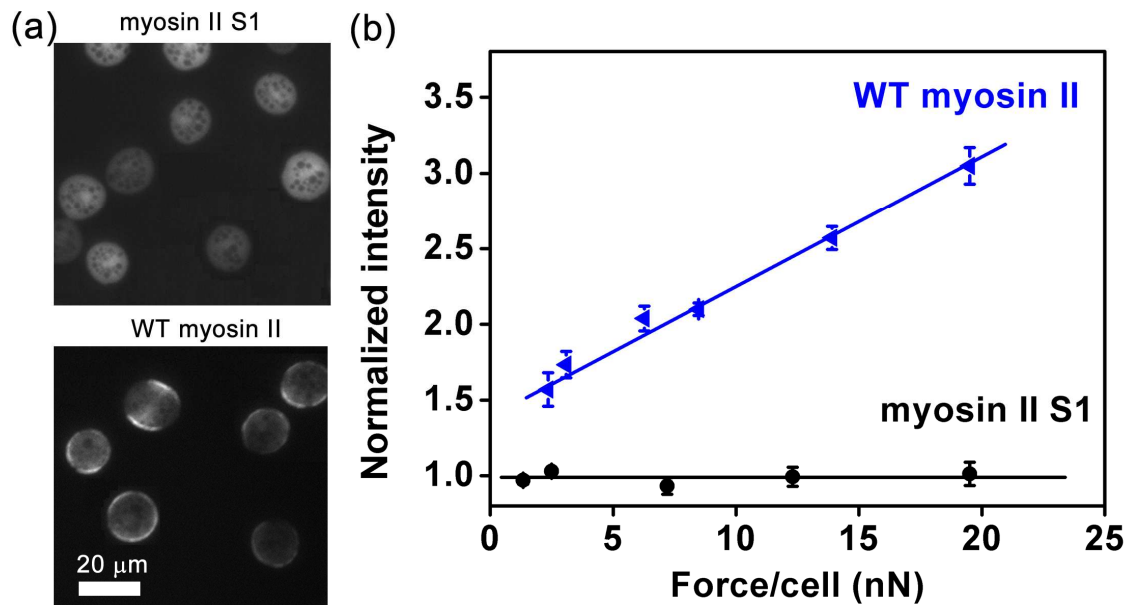
Figure S9. The comparison of the mechanosensory response between WT myosin II and myosin S1. **(a)** The representative fluorescent images of compressed cells expressing myosin II S1 and WT myosin II. **(b)** The normalized intensity of accumulated WT myosin II and myosin II S1 during compression. Here, the myosin S1 is monomeric and does not have the assembly domain so that it cannot assemble into bipolar thick filaments and generate contractile force. The error bars in **(b)** represent the standard error of mean.
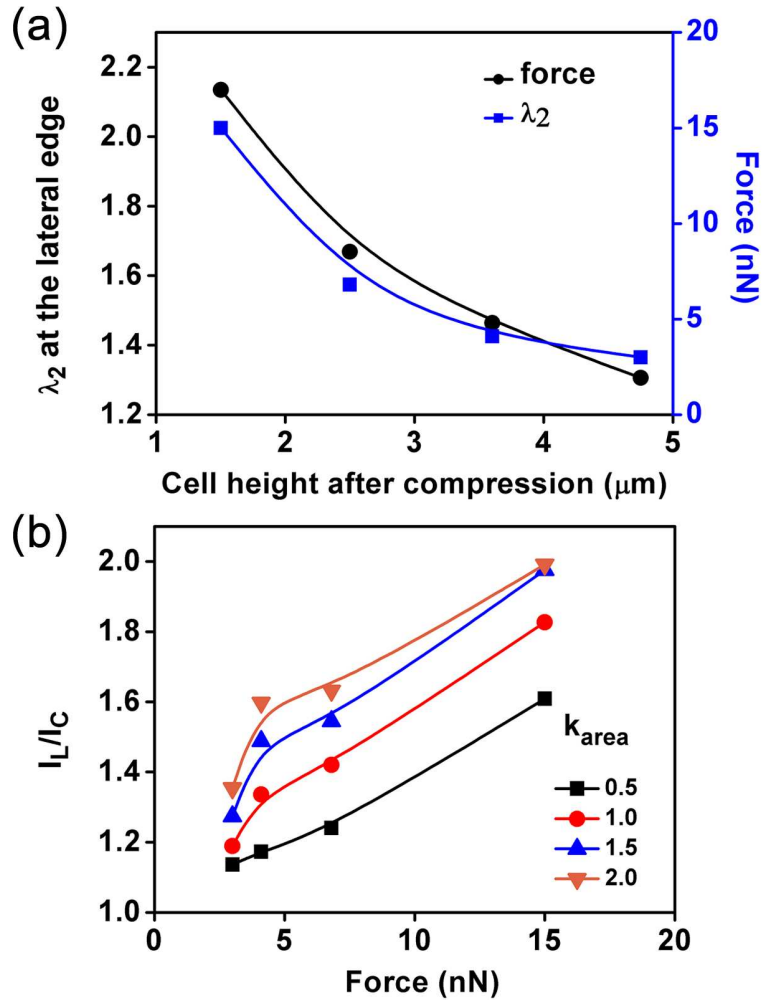
Figure S10. The simulated force-accumulation relation based on STZC model: **(a)** the relation among compression force, cell height and λ_2 at the lateral edge (maximum value); **(b)** the simulated accumulation of myosin II for various k_{area}.
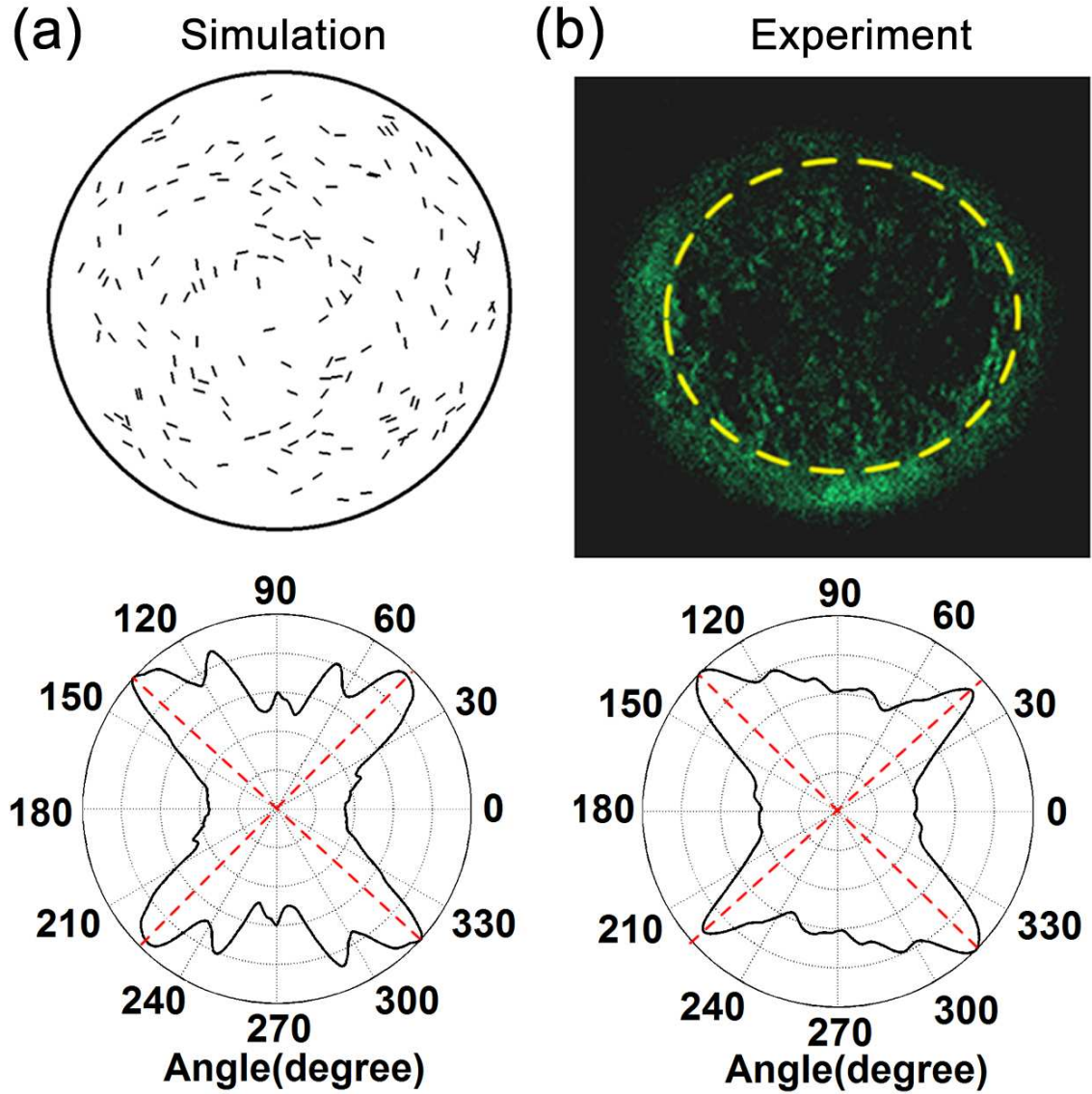
Figure S11. The comparison of the distribution of myosin bipolar thick filaments in the simulation **(a)** and experiment **(b)**. The lower panels are the angle distributions of the bipolar thick filaments shown in the upper panels. For the experiment, only the filaments outside the middle plane of the compressed cell (enclosed by the yellow circles) are taken into account. The angle distributions of the filaments in both simulation and experiment mainly peak around ±45° (indicated by the red broken lines) with respect to the radical direction (0°-180° axis). The upper panel of (a) is the same as Fig. 6e where β=4.
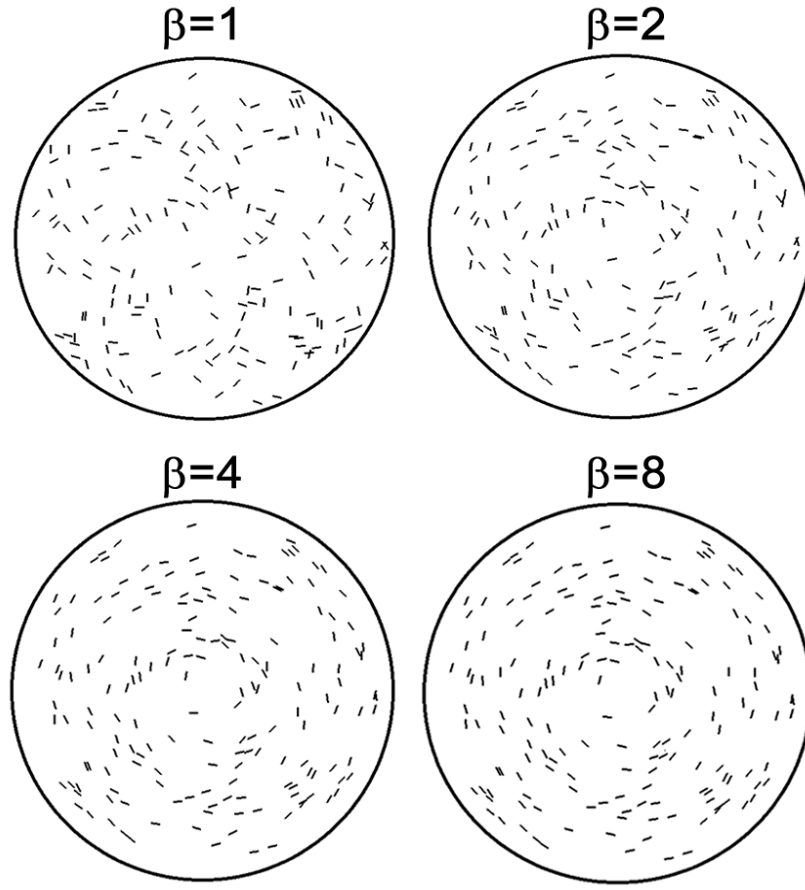
Figure S12. The polarization of myosin II BTFs due to compression. The angle deviated from the radical direction is $\xi=\tan^{-1}(\beta\lambda_2/\lambda_1)$. β characterizes the effect of the ratio of principal strains on ξ.
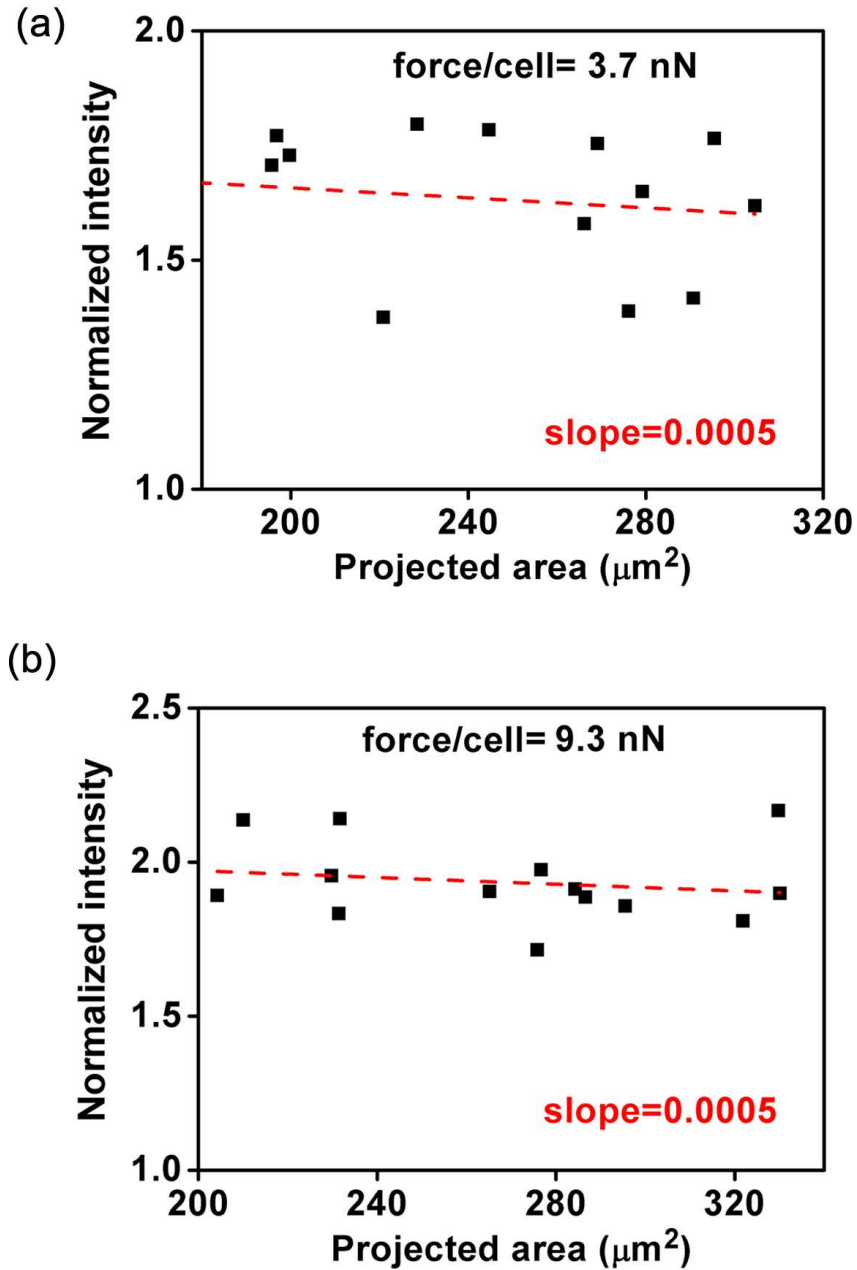
Figure S13. The accumulation of wide-type myosin II doesn't correlate with the volume of cells under different compression forces: **(a)** 3.7 nN and **(b)** 9.3 nN. For the compressed cells imaged underneath the same agarose sheet, the projected area of each cell is the measure of the cell volume as the cell shape is close to a pan-cake and the heights of the cells are the same. The correlation coefficients (the slopes) in **(a)** and **(b)** are almost zero, suggesting that there is no correlation between the mechanosensitive accumulation of myosin II and the cell volume.

3. Supplementary movie

Movie S1: A 3D-rendered view based on the stacking of a series of confocal images taken from different focal plane of a compressed cell expressing GFP-myosin II.

Supplementary References

1.   Rivlin, R. S., Large Elastic Deformations of Isotropic Materials. I. Fundamental Concepts. *Philos. Trans. R. Soc. London, Ser. A* **1948,** *240* (822), 459-490.

2.   Mooney, M., A Theory of Large Elastic Eeformation. *J. Appl. Phys.* **1940,** *11*, 582-592.

3.   Liu, K. K.; Williams, D. R.; Briscoe, B. J., Compressive Deformation of a Single Microcapsule. *Phys. Rev. E* **1996,** *54* (6), 6673-6680.

4.   Skalak, R.; Tozeren, A.; Zarda, R. P.; Chien, S., Strain Energy Function of Red Blood Cell Membrane. *Biophys. J* **1973,** *13*, 245-264.

5.   Yang, W. H.; Feng, W. W., On Axisymmetrical Deformations of Nonlinear Membranes. *J. Appl. Mech.* **1970,** *37*, 1002-1011.

6.   Feng, W. W.; Yang, W.-H., On the Contact Problem of an Inflated Spherical Nonlinear Membrane. *J. Appl. Mech.* **1973,** *40*, 209-214.